

A Scanning Transfer Cavity Frequency Lock for Experimental Quantum Information

by
Katherine S. Collins

A senior honors thesis submitted to the
Department of Physics, University of Maryland, College Park
in partial fulfillment of the requirements for the degree of
Bachelor of Science in Physics, with High Honors
2017

Defense Committee:

Professor Christopher R. Monroe, Chair

Professor Steven M. Anlage

Professor Gretchen K. Campbell

For my mother, Lisa

Acknowledgements

I am truly grateful to Chris Monroe for introducing me to the quantum systems of trapped ions. Being mentored by him as an undergraduate researcher in the Trapped Ion Quantum Information group has been an extraordinary dream come true. Chris, thanks for taking a chance on a no-nothing Freshman.

Many thanks to Kristi Beck for all of her help and tireless guidance in conducting, drafting, and writing my senior thesis. I have learned so much from you.

I want to also thank Ken Wright for, in fact, teaching me all of the physics and experimental research skills that I know. I would not have had the best undergraduate research experience imaginable without your patience, support, and inclusiveness.

To the other members of the Chip Lab, Daiwei Zhu and Sid Harmalkar, I have really enjoyed working with each of you. Daiwei, you have taught me your favorite word “dank” which is equivalent to “really awesome” and I know you will be a great senior graduate student in Chip Lab. Sid, I know you will have as amazing a research experience as I have had.

I also want to thank all of the members of the Trapped Ion Quantum Information group, both current and past, for their help, and for taking the time to answer the countless physics questions I pestered you with. It was a fantastic experience working with you all.

To my good and long time friend Emily Ackerman, thank you for your support, and for being there at a moment's notice. Thank you to David, Sherry, Odette, Efrain and my extended family, for being in my life and providing friendship over the years.

Most of all, thank you to my Mom. I am grateful for all of the opportunities, the endless support, and the love you have given me. I am lucky to have been adopted by you and that you became my Mom. In the ultimate roll of the dice, you refused the Welfare Institute's effort to swap me out for a “healthy girl,” instead choosing to stick with the “sick one.”

Contents

Dedication	ii
Acknowledgements	iii
List of Tables	vi
List of Figures	vii
Abstract	viii
1 Introduction	1
2 Frequency Stabilization Lock	6
3 Experimental Setup	9
3.1 Scanning Transfer Cavity Design	9
3.2 Transfer Cavity & KF Vacuum Assembly	13
3.3 Optical Setup & Detection	18
3.4 Coupling Optics for Mode-Matching	24
4 Measurements & Results	30
5 Discussion & Conclusion	37
Appendix A Lists of Components	40
A.1 Lasers & Wavemeter	40
A.2 Transfer Cavity	40

A.3 KF Vacuum Chamber	40
A.4 Complete Optical Setup	42
Appendix B Diagrams & Drawings	43
B.1 Ytterbium-171 Energy Diagram	43
B.2 INVAR Spacer	44
B.3 Transfer Cavity Assembly Jigs	45
B.4 Vacuum Window Holders	46
B.5 KF Vacuum Chamber Base	47
B.6 KF Vacuum Chamber Lid	48
Appendix C Component Specifications & Manuals	49
C.1 Vacuum Components	49
C.2 Accu-Glass Products, Inc.	49
C.3 American Piezo Ceramics, Ltd.	49
C.4 Lambda Research Optics Transfer Cavity Mirrors	49
C.5 Semrock	50
C.6 Thorlabs	50
C.7 Allied Vision Technologies	51
References	52

List of Tables

1.1	$^{171}\text{Yb}^+$ CW Laser Frequencies & Natural Linewidths	3
3.1	Laser Powers at the Input of the Transfer Cavity	20
3.2	PDA36A Si Adjustable Gain Photodetector Responsivity	21
3.3	Photodetector Gain Settings	21
3.4	Voltage Signal Ratios	22
3.5	Voltage Signals Ratios with the Addition of the Two Bandpass Filters	23
3.6	Mode-Matching Beam Widths	26
3.7	Focal Lengths of Mode-Matching Coupling Optics	28
4.1	Mean, Standard Deviation, & Variance in Ion Fluorescence Data Sets	33
4.2	Linear Fit Parameters for “Converting from MHz to kCounts/s”	34
4.3	Relative Frequency Stability of the 369 nm Laser Standard Deviation & Variance	36

List of Figures

1.1	Ytterbium-171 Energy Diagram	2
2.1	Resonant Transmission Peaks	6
3.1	Transfer Cavity	9
3.2	Stability Diagram of an Optical Resonator	12
3.3	Transfer Cavity Vacuum Chamber Housing	15
3.4	Initial Setup of Transfer Cavity System	18
3.5	Gaussian Beam Widths of Transfer Cavity	26
3.6	Telescope Mode-Matching Coupling Optics	27
3.7	Final Optical Setup of Transfer Cavity System	29
4.1	Cooling Frequency Calibration Curve	31
4.2	Measured Ion Fluorescence using Different Frequency Locks	32
4.3	Linear Fit	34
4.4	369 nm Laser Short Term Frequency Stability	35
B.1	Detailed $^{171}\text{Yb}^+$ Energy Level Diagram	43
B.2	INVAR Rod Drawing	44
B.3	Transfer Cavity Assembly Jigs	45
B.4	Transfer Cavity Chamber Window Holders	46
B.5	KF Vacuum Chamber Base	47
B.6	KF Vacuum Chamber Lid	48

Abstract

For many atomic, molecular, and optical physics experiments, stabilized lasers are a vital necessity, especially if specific frequencies are used to trap, cool, and drive optical transitions corresponding to a system of atoms. Frequency stabilization within a fraction of the transition linewidth and suppression of frequency drifts greater than 1 MHz, in general, utilizes a laser referenced to a strong atomic transition to lock and control the frequencies of lasers that are not stable. This senior thesis presents the physical implementation of an evacuated scanning transfer cavity with a free-spectral range (FSR) of ~ 786 MHz to stabilize and lock the different frequencies corresponding to the optical transitions of Ytterbium-171 ($^{171}\text{Yb}^+$) ions. The FPGA-based peak detection frequency stabilization lock is currently being worked on using a laser frequency that is stabilized to the strong atomic $F = 2 \rightarrow F' = 3$ cycling transition of Rubidium-87 (^{87}Rb). We present short-term frequency stability measurements of the 369 nm laser that is locked via the transfer cavity system by looking at the ion fluorescence of a single trapped ion while the 399 nm and 935 nm lasers are locked using our current locking method via a commercially-available calibrated wavemeter.

1 Introduction

In experimental atomic, molecular, and optical (AMO) physics, the use of a laser or several lasers are crucial tools. A laser with a frequency corresponding to the difference in energy between two different electronic states of an atom can drive stimulated transitions between those two energy levels. The quantization of the atom's energy levels requires a specific laser frequency to make the corresponding transition within the transition linewidth. For example, typical linewidths of atomic transitions used for laser cooling are on the order of MHz. [1] As a result, a stable laser frequency is of great importance. Unfortunately, the frequency of a laser does not stay at a constant value but instead has a tendency to drift away from the desired value. Temperature fluctuations will change the grating position of an external cavity diode laser (ECDL). All frequency drifts greater than 1 MHz are quite problematic in AMO experiments that utilize particular laser frequencies such as for trapping, cooling, and manipulating neutral atoms or ions.

Fortunately, many solutions exist, and in general, a reference frequency source and a locking-feedback system is utilized to stabilize laser frequencies and control frequency drifts to about 1 MHz or less. [2, 3] Frequency stabilization methods differ primarily in the source of the strong atomic transition (reference frequency) such as using an atomic vapor cell [4], or a hollow-cathode lamp [5, 6]. A commercially-available wavemeter can also be used to measure and lock laser frequencies. Another solution consists of implementing a stabilized transfer cavity system. [7–11] A reference laser with a frequency stabilized to a strong atomic transition is aligned and coupled to a transfer cavity. Another laser frequency that is not-so-stable is also coupled to the transfer cavity. The output cavity frequency signal of this laser can be locked to the cavity-coupled signal of the reference laser. This method allows the stability of the reference laser to be transferred via the cavity to the unlocked laser resulting in the ability to setup a stabilized frequency lock and feedback system.

For the past two-and-a-half years, I have had the amazing opportunity to conduct research in Dr. Christopher Monroe's Trapped Ion Quantum Information group at the Joint Quantum Institute. Our group's research involves trapping Ytterbium-171 ($^{171}\text{Yb}^+$) ions and manipulating the internal states of these atoms as an experimental platform for quantum computations and simulations.

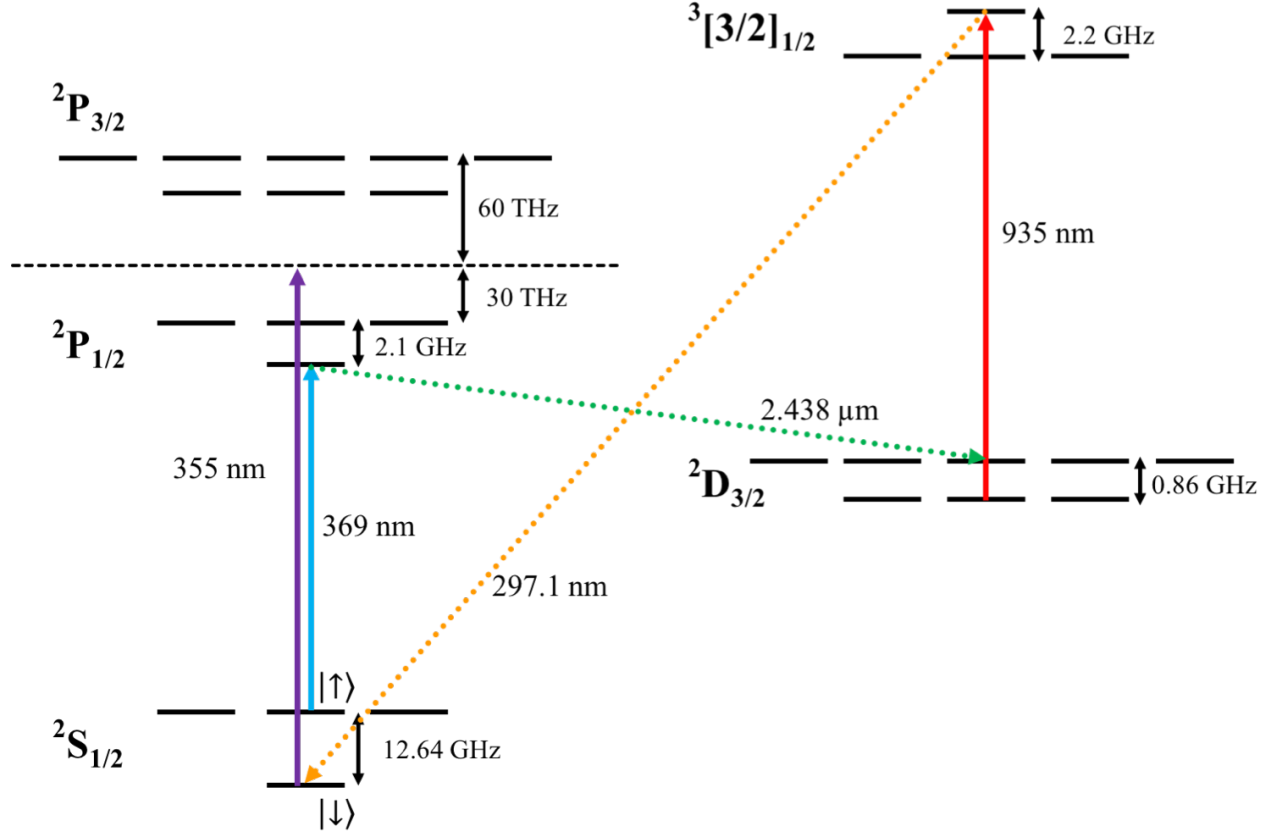


Figure 1.1. Ytterbium-171 Energy Diagram: Lasers are used to manipulate the electronic states of $^{171}\text{Yb}^+$ and to trap and cool the ions. The 369 nm, 399 nm (not shown in the diagram), and 935 nm are continuous-wave lasers while the 355 nm wavelength originates from a mode-locked high power pulsed laser.

Fig.1.1 shows a simplified energy diagram of $^{171}\text{Yb}^+$ in which lasers are used to drive allowed optical transitions between different states. The wavelengths of these lasers and the driven transition are represented by the vertical solid-colored arrows. Spontaneous emission transitions are represented as dashed arrows. A more detailed $^{171}\text{Yb}^+$ energy level diagram

can be found in Appendix B. A laser at a wavelength of ~ 399 nm, not depicted in Fig. 1.1, is used to excite a beam of neutral Yb atoms from the 1S_0 level to the 1P_1 level, a process in which one photon is emitted per excited atom. The 369 nm laser will complete the two-photon transition photoionization of Yb atoms. The 369 nm laser is also used for Doppler cooling, optical pumping (state detection), and state preparation of $^{171}\text{Yb}^+$. Finally, for any population that state, the 935 nm laser will re-pump any population that spontaneously decays from the $^2P_{1/2}$ state into the $^2D_{3/2}$ to the bracket state $^2[3/2]_{1/2}$. This bracket state has a significantly shorter lifetime than the $^2D_{3/2}$ state and has a very high probability of decaying back into the ground state.[12] These three lasers — 369 nm, 399 nm, and 935 nm — are all continuous-wave (CW) external cavity diode lasers. The other transition represented in Fig. 1.1 (the purple arrow) corresponds to the stimulated Raman transitions between the two hyperfine $m_f=0$ levels of the $^2S_{1/2}$ ground state. The 355 nm resonant transition represents the difference between two detuned frequencies that are generated by a pulsed laser which is not locked to a stabilized reference source. Instead, the lasers are mode-locked by stabilizing their beat-note frequency. [13]

Currently, we use a commercially-available wavemeter [14] to measure and display the frequencies of the 369 nm, 399 nm, and 935 nm lasers which are listed below in Table 1.1. Table 1.1 also displays the natural linewidth of the corresponding optical transition that each laser addresses.

Table 1.1. $^{171}\text{Yb}^+$ CW Laser Frequencies & Natural Linewidths:

λ	ν	$\Gamma/2\pi$
369 nm	~ 811.289444 THz	~ 20 MHz
399 nm	~ 751.527546 THz	~ 28 MHz
935 nm	~ 320.569211 THz	~ 4.2 MHz

The wavemeter is calibrated to a reference frequency which is stabilized to the strong atomic $F = 2 \rightarrow F' = 3$ cycling transition of Rubidium-87 (^{87}Rb) corresponding to the frequency of 384.228115 THz (wavelength of 780 nm).[15] Our CW lasers are locked using the calibration and measurement settings of the wavemeter. The wavemeter frequency lock works well and has provided us a handy tool to measure the frequencies of our lasers, but there are some limitations. The wavemeter readings appear to be very sensitive to ambient noise, temperature, and pressure. For example, we observe variations in the frequency readings of our lasers that limit us in shot to shot detection in our experiments. In addition, the noise that we observe is not reproducible from shot to shot. The fluctuations in the measurements of the frequencies is larger than we need it to be if we wanted to be able to sit on the ion's linewidth.

The initial idea and project of implementing a scanning transfer cavity frequency stabilization lock originated before I joined the Trapped Ion Quantum Information group (which was almost three years ago) and before the experiment that I've been a part of had a wavemeter. The motivation for implementing the transfer cavity system has gained more interest lately since we have noticed issues with the wavemeter. Based on the designs of our transfer cavity system, using an evacuated cavity, we expect the stability in the frequency lock to be similar to the performance of the wavemeter but with less sensitivity to the ambient environment of the lab. The rest of this thesis will talk about my work implementing the physical setup of a stabilized scanning transfer cavity system in order to stabilize and lock the three CW lasers — 369 nm, 399 nm, and 935 nm — of $^{171}\text{Yb}^+$. The structure of this thesis is as follows:

- Ch. 2 describes the general idea of the frequency lock and feedback method that we plan to use as well as our reasoning for placing the transfer cavity under vacuum instead of using it in ambient lab conditions.
- Ch. 3 details the design of the transfer cavity and its properties.

- Ch. 4 discusses the assembly of the transfer cavity, the KF vacuum chamber, and the placement of it under vacuum.
- Ch. 5 outlines the main components of the transfer cavity optical layout and discusses the detection of the cavity-coupled laser signals.
- Ch. 6 talks more specifically about the mode-matching optics needed to couple the three $^{171}\text{Yb}^+$ lasers (369 nm, 399 nm, and 935 nm) and the reference laser (780 nm) to the transfer cavity.
- Ch. 7 presents the first set of measurements and results of the stability of the transfer cavity frequency lock and compares its performance to the current performance of the wavemeter.
- Ch. 8 summarizes the current status of our transfer cavity frequency stabilization system and discusses future directions to be taken to obtain a higher degree of frequency stabilization.

2 Frequency Stabilization Lock

The three CW $^{171}\text{Yb}^+$ lasers (369 nm, 399 nm, and 935 nm) and the stabilized reference laser (780 nm) are all aligned to the input mirror of the scanning transfer cavity. At the output of the transfer cavity, the transmitted laser signals are all aligned to their own photodetector. Fig.2.1 displays the cavity-coupled resonant transmission peaks of the four lasers as one length of the cavity is swept over once.

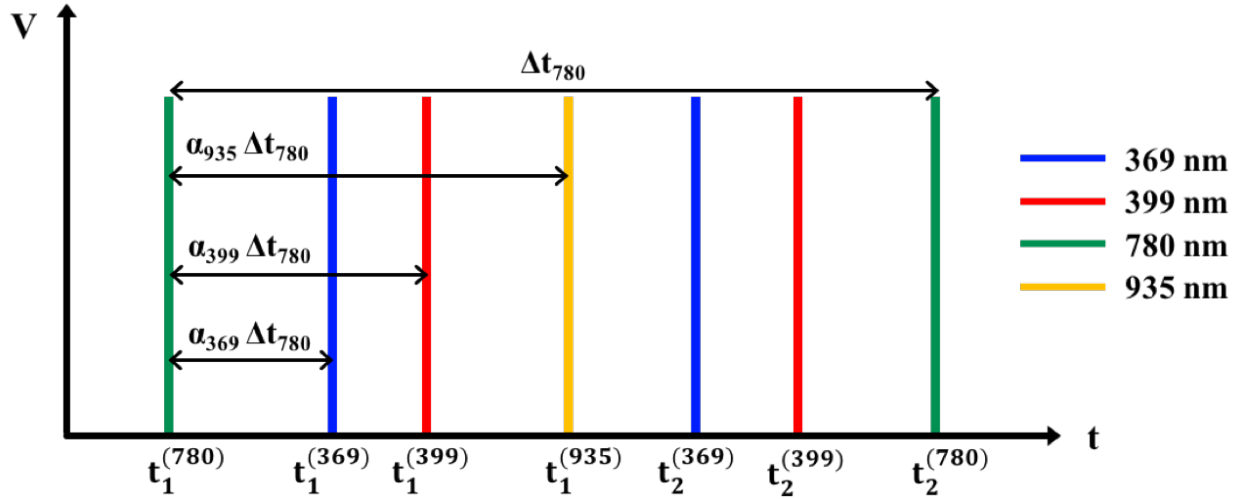


Figure 2.1. Resonant Transmission Peaks: The transmission of light from the scanning transfer cavity will be nonzero only when the frequency of the light is resonant with the fundamental cavity mode as the length of the cavity is swept over in time.

Our frequency stabilization lock is achieved using a FPGA-based solution in which the resonant signals measured by the four photodetectors, shown in Fig.2.1, are sent to an analog-to-digital converter in order to be read by the FPGA. For each scan over the cavity length, the FPGA will be prompted to find the times corresponding to the maximum resonant transmission peaks of the 780 nm laser and the first maximum resonant transmission peak of the 369 nm, 399 nm, and 935 nm laser signals. These resonant peak times are also labeled in Fig. 2.1.

More specifically, an error signal will be generated for each $^{171}\text{Yb}^+$ frequency in order to maintain a constant value for α_λ which is defined by the following equation:

$$\alpha_\lambda = \frac{\Delta t}{t_{FSR}^{(780)}} = \frac{t_\lambda - t_1^{(780)}}{t_2^{(780)} - t_1^{(780)}} \quad (2.1)$$

where t_λ is the time corresponding to the first TEM_{00} transmission peak of the specified $^{171}\text{Yb}^+$ laser, and the parameters $t_1^{(780)}$ and $t_2^{(780)}$ are the times of the 780 nm laser TEM_{00} peaks. The time difference between $t_1^{(780)}$ and $t_2^{(780)}$ is a measurement of the free-spectral range (FSR) of the transfer cavity. Three α_λ values, one for each $^{171}\text{Yb}^+$ laser, will be compared to the previous value for each full piezo scan of the length of the transfer cavity. By feeding back the error signal generated for each $^{171}\text{Yb}^+$ laser to the corresponding laser controller box piezo, we hope to minimize long-term frequency drifts and successfully stabilize each frequency after conducting a full optimization of the transfer cavity system.

S. Uetake *et al.* [10] discuss frequency stabilization performance limitations in using a non-evacuated transfer cavity mainly due to the frequency dependence of the index of refraction of air and derive a relationship between the wavelengths of the slave and master lasers, Eq.(2.2), assuming that both lasers satisfy the resonant conditions of the transfer cavity.

$$\lambda_s = \lambda_m \frac{n_s}{n_m} \frac{2 N_m + \alpha}{2 N_s} \quad (2.2)$$

In Eq.(2.2), N denotes the resonant mode number, λ denotes the wavelength of the laser, n denotes the index of refraction of air which is dependent on wavelength, and subscripts m and s denote the master and slave lasers. The maximum relative fluctuation of the slave laser is given by

$$\left| \frac{\delta \lambda_s}{\lambda_s} \right| \leq \left| \frac{\delta \lambda_m}{\lambda_m} \right| + \left| \frac{\delta \alpha}{2 N_m + \alpha} \right| + \left| \frac{\delta n_s}{n_s} - \frac{\delta n_m}{n_m} \right| \quad (2.3)$$

in which the first term on the right-hand side is the relative fluctuation of the master laser, the second term corresponds to the residual drift of the locking method, and the third term is the residual drift of the index of refraction of air for the master and slave wavelengths. The second and third terms in Eq.(2.3) need to be as small as possible in order for the stability of the master laser to be transferred to the slave laser. [10] The second term can be reduced by increasing the spectral resolution of the transfer cavity lock system while the third term in Eq.(2.3) results in the main limitation to the performance of the frequency stabilization of a non-evacuated transfer cavity. This term will never be zero for such a transfer cavity since the index of refraction is dependent on ambient room conditions. [16,17] However, using an evacuated cavity to transfer the frequency stability of the master laser to the slave laser will reduce the third term in Eq.(2.3). [10] We chose to place our transfer cavity under vacuum in order to minimize the frequency dependency of the index of refraction of air. [16,17] From [7] and [10] we believe that using an evacuated cavity will enable us to obtain frequency stability for the three $^{171}\text{Yb}^+$ lasers.

3 Experimental Setup

3.1 Scanning Transfer Cavity Design

Our optical resonator is a scanning hemi-plano-concave cavity shown in Fig. 3.1. The physical length, L , of the cavity is 190.815 mm, which is the sum of the lengths of the cylindrical piezoelectric tube, L_{piezo} and the machined INVAR rod, L_{INVAR} .

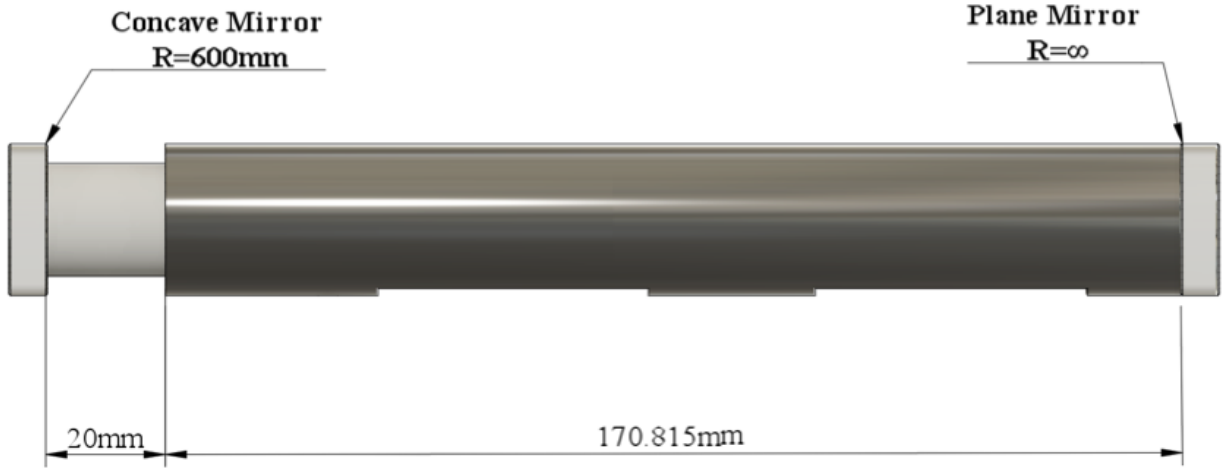


Figure 3.1. Transfer Cavity: A CAD model of our hemi-plano-concave scanning transfer cavity is shown above. The two piezo wires that are soldered to its inner and outer cylindrical surfaces are not depicted. The spherical concave mirror with a radius of curvature of 600 mm is Torr-Sealed to the piezo while the flat mirror is Torr-Sealed to the other end of the INVAR rod.

The piezoelectric (piezo) cylindrical tube is composed of high purity lead zirconate titanate ceramic from APC International, Ltd. and has a specified length, L_{piezo} , of 20 mm. The piezo is Torr-Sealed between the faces of the curved mirror and the INVAR rod. Not depicted in Fig. 3.1 are the two wires that are soldered to the piezo, one to the inside surface and one to the outer cylindrical surface. The piezo's inner surface is positively polarized. The other ends of the inside and outside wires of the piezo are connected to a female BNC connector head in which the inside wire is connected to the center pin of the BNC and the outside wire

is connected to the outer pin. A SRS function generator is used to produce a triangular ramp that is amplified by a high-voltage (HV) source in order to drive the piezo. BNC cables are used to connect the output signal of the function generator to the input of the HV amplifier and from the output of the HV amplifier to the BNC connector head of the transfer cavity chamber.

The transfer cavity body is a custom-machined INVAR rod that was designed by former members of Dr. Monroe's group. As shown in Fig. 3.1, the INVAR spacer is 170.815 mm long (L_{INVAR}). The outer diameter of the spacer is 25.4 mm and the inner diameter is 12.7 mm. The INVAR has two rectangular sections that have been cut into the surface of the rod, and both are centered with an 8-32 threaded hole. This feature defines the bottom of the cavity which allows the ability for the cavity to be mounted on two optical posts. In addition, a small hole has been drilled through the bottom side of the cavity near one end, allowing the wire soldered to the inside surface of the piezo to be fed out of the spacer once the piezo is Torr-Sealed to the radial face of the cavity. Since we planned to place our transfer cavity under vacuum, we drilled an additional small hole through the bottom of the INVAR in order to provide another outlet for molecules to be pumped out of and evacuated from the inside of the cavity. INVAR was chosen as the material of the rod since it has a very low thermal expansion coefficient in comparison to other metals. [18]

The transfer cavity mirrors, a spherical plano-concave, mirror and a flat mirror were custom-ordered from Lambda Research Optics, Inc. The radius of curvature of the concave mirror is 600 mm, which is just over a factor of three times greater than the length of the cavity. Both mirrors are fused silica glass, 25.4 mm in diameter, and are 6.35 mm thick. In addition, each mirror has surface coatings on each side. The outer planar faces of the mirrors have an anti-reflection coating with a quoted reflectivity of less than 0.5 % for wavelengths between 369 nm to 399 nm and 780 nm to 935 nm. The inner mirror faces, the concave and plane

surfaces, have a high reflective coating in which the quoted 369 nm and 780 nm reflectivity coefficients are greater than 99 % while the 399 nm and 935 nm reflectivity coefficients are greater than 98 %. The reflection coefficients mentioned for each surface are quoted for angle of incidences of 0° .

An optical cavity is considered a stable resonator if the following inequality is satisfied:

$$0 \leq g_1 g_2 \leq 1 \quad (3.1)$$

in which g_1 and g_2 are dimensionless stability parameters relating the ratio of the cavity length, L , to each mirror's radius of curvature, $R_{1,2}$ (see Eq.(3.2).)

$$g_{1,2} = \left(1 - \frac{L}{R_{1,2}}\right) \quad (3.2)$$

A full derivation of Eq.(3.1) using the paraxial approximation and ABCD transfer matrices can be found in [23]. For our hemi-plano-concave cavity, the stability g-parameters are:

$$g_1 = \left(1 - \frac{190.725 \text{ mm}}{600 \text{ mm}}\right) = 0.681975 \quad (3.3)$$

$$g_2 = \lim_{R_2 \rightarrow \infty} \left(1 - \frac{L}{R_2}\right) = 1 \quad (3.4)$$

Substituting Eq.(3.3) and Eq.(3.4) into Eq.(3.1):

$$0 < (0.681975)(1) \leq 1, \quad (3.5)$$

we show that our transfer cavity is a stable resonator since it satisfies the stability condition, Eq.(3.1). Fig. 3.2 displays a graph of the stable and unstable optical resonators in which the coordinate axes are the two g-parameters, g_1 and g_2 . The stability of our cavity lies within the blue-shaded region of the first quadrant.

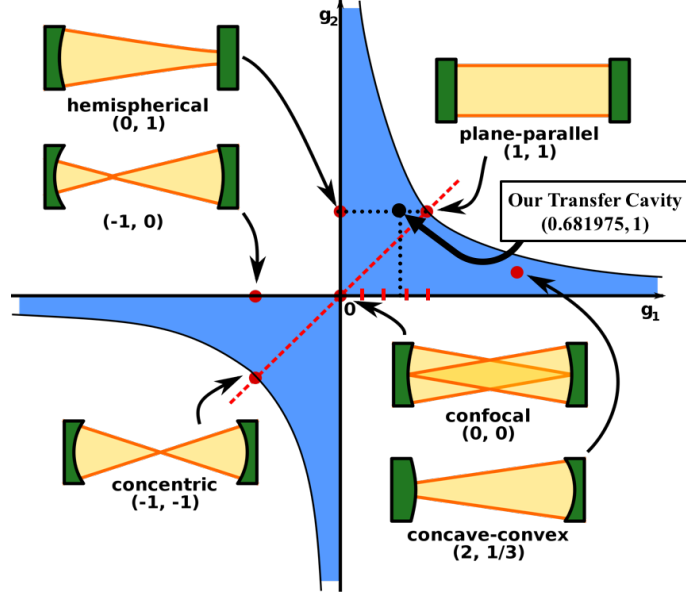


Figure 3.2. Stability Diagram of an Optical Resonator: The stability diagram displays several examples of stable cavities. [19] We modified this diagram by indicating the location that our transfer cavity (the black circle) with respect to the other designs.

The FSR of an optical cavity is defined by the following equation,

$$\nu_{FSR} = \frac{c}{2L} \quad (3.6)$$

where c is the speed of light in vacuum and L is the distance between the two cavity mirrors.

Using Eq.(3.6) and substituting in $L = 190.815$ mm for our cavity, we calculate a FSR of ~ 785.6 MHz. The finesse of an optical cavity is given by the following equation

$$\mathcal{F} = \frac{\nu_{FSR}}{\nu_{FWHM}} = \frac{\pi(\mathcal{R}_1\mathcal{R}_2)^{1/4}}{1 - (\mathcal{R}_1\mathcal{R}_2)^{1/2}} \quad (3.7)$$

where \mathcal{R}_1 and \mathcal{R}_2 are the reflectivity coefficients of each mirror and ν_{FWHM} is the full-width-half-maximum (FWHM) of the transmission peaks. If the finesse and FSR are known of the cavity Eq.(3.7) can be rearranged to calculate the FWHM of the resonant transmission peaks for a given wavelength, λ .

3.2 Transfer Cavity & KF Vacuum Assembly

Clean-room and vacuum procedures were followed while building the transfer cavity and assembling the cavity vacuum chamber. Lists of the assembly components for both the transfer cavity and its housing can be found in Appendix A. Drawings and other data specifications of the transfer cavity and chamber parts are given in Appendix B and Appendix C. In addition, a drawing of the two simple metal assembly jigs — a mirror jig and a piezo jig — are also included in Appendix B. These two assembly jigs were designed to aid in centering and aligning the cavity mirrors, cylindrical piezo tube, and INVAR spacer with each other so that cavity modes are supported. From previous experience, a cavity that has misaligned mirrors with respect to the optical axis of the system will not demonstrate any mode structure when trying to couple a laser to the cavity. This chapter highlights a few notes of importance regarding the building of the cavity and obtaining a stable vacuum system.

The impedance of the piezo is large, on the order of $\gtrsim 50\text{ M}\Omega$. Using a Fluke 179 True RMS multimeter, the measured resistance of the piezo should read overload ('OL') where the maximum resistance specified for this multimeter model is $50\text{ M}\Omega$. [20] The two ultra-high vacuum (UHV) compatible copper-insulated 34 AWG wires are soldered onto the piezo using a UHV-compatible soldering iron and UHV in-vacuum solder. The temperature of the iron can be adjusted so that it is hot enough to make a good solder joint between the piezo and the wire, but not so hot that it melts the electrode-coated surfaces of the piezo. The latter is very easy to do if the iron is in contact with the piezo for too long and/or at too high a temperature. The inside piezo wire should be attached first and confirmed that it is electrically-connected before Torr-Sealing the piezo to the curved face (indicated on the mirror side by penciled arrow) of the plano-concave mirror. It helps to cut the copper wires slightly long since they can easily be shortened at the end of the assembly process.

A longer inside piezo wire assists with feeding that wire through the small through-hole in the INVAR rod and adjusting it such that it lies as flat as possible before the INVAR rod is placed in contact with the other end of the piezo with Torr-Seal. The outside wire should be soldered at the very end of the physical transfer cavity assembly once all the Torr-Seal has completely potted. The impedance of the piezo should be remeasured and verified that it is still significantly larger than $50\text{ M}\Omega$. If the multimeter resistance reading is still ‘0L’, then this measurement implies that the piezo is not shorted to the INVAR spacer and the transfer cavity is ready to be optically aligned to ensure that cavity mode-structure can be detected.

However, if the impedance of the piezo is on the order of $\sim 2\text{ }\Omega$, then this implies that the piezo is likely shorted to the INVAR or damaged (*i.e.* de-polarized). We encountered a situation in which the wire connected to the inner surface of the piezo was shorting to the INVAR. Some of the enamel of the wire had been scrapped off and was in contact with the INVAR as the wire was going through the small hole. Fortunately, we were able to fill the hole with Torr-Seal and position the inside wire such that the scraped-off enamel was no longer in contact with the INVAR and that a high impedance was still measured. For future cavity constructions, make sure that the thru-hole is de-burred and/or use UHV-compatible wires with a thicker insulation.

The cavity housing design consists of KF-components except for the Agilent VacIon 21/s mini ion pump that has a CF-flange. The transfer cavity rests on a groove that is inside the rectangular base of the chamber. It is not tied down in any way except by the effect of gravity, so one needs to be careful when moving the chamber, such as from the bake-out location to the optics table. The transfer cavity chamber housing is shown on the next page in Fig. 3.3.

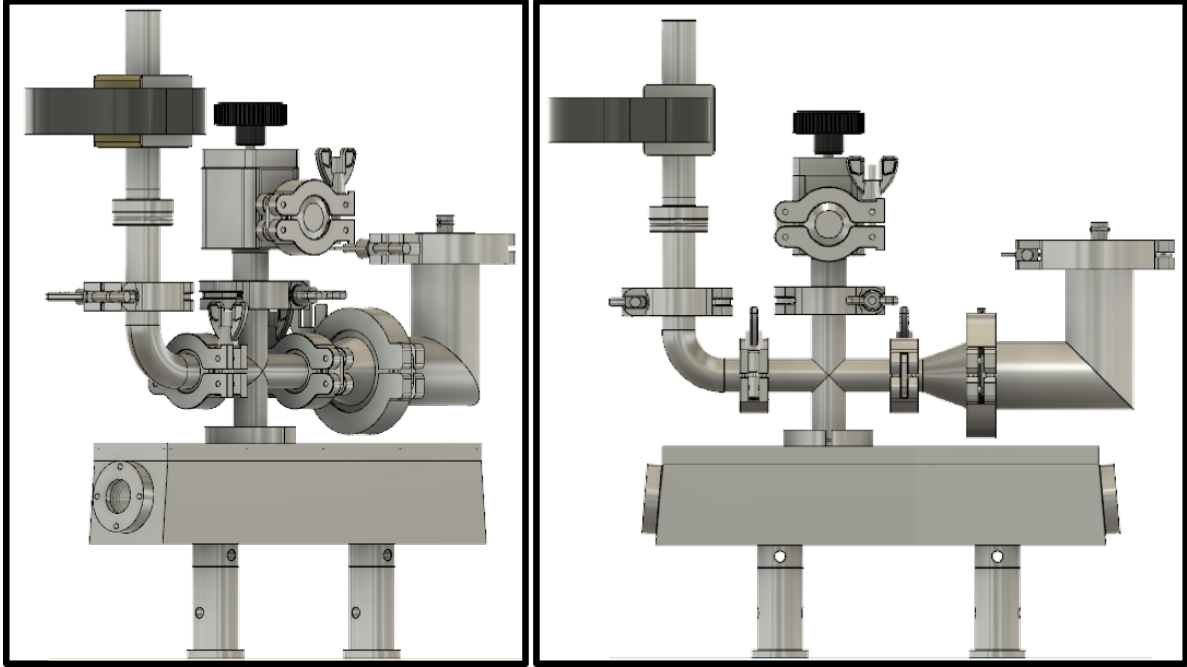


Figure 3.3. Transfer Cavity Vacuum Chamber Housing: Two perspectives of the transfer cavity vacuum chamber are shown. The image on the left provides an angled perspective of the chamber while the image on the right gives an orthographic side-view of the housing. The input of the cavity (location of the curved mirror and piezo) corresponds with the end of the chamber that has the mini-ion pump and U-shaped magnet while the output of the cavity (location of the plane mirror) is on the other end of the chamber where the BNC cable can be plugged into the top of the mitered-elbow connection. The inside and outside piezo wires are connected to this BNC bulkhead. This chamber was designed by a past post-doc of our group and was built by another graduate student in the lab. Not shown in either of the images is the HV connection that slides over top the short vertical tube located just above the magnet. On the other end of this connection is the MiniVac ion pump controller that indicates the current of the mini-ion pump.

In our first few attempts to bake the chamber, we initially had a small Thorlabs breadboard lying on top of oven blocks with the chamber posts tied down to the breadboard. This setup was not a good plan since we created a very large thermal gradient (the breadboard) underneath a high conductance system which resulted in broken chamber windows at about 35–40 °C. Thus, it is important to not use a breadboard when baking but instead to just to zip-tie down the chamber and cover the optical posts with aluminum foil.

The cavity chamber was baked at a temperature of $\sim 70^\circ\text{C}$ for about two weeks. Once the temperature of the system was at room temperature, we made sure that the ion pump could continue pumping the system on its own without the turbo pump by closing the valve. In addition to the MiniVac controller which monitors the ion pump current, we measured the ion-pump voltage in order to determine if we would be able to turn off and disconnect the turbo pump. After this initial bake, the ion pump voltage was stabilized at about 50 mV and was successfully transferred over to the optics table. However, over a time span of about six months, we noticed that there was a very slow leak from our vacuum chamber where the voltage had gradually reached $\sim 80\text{ mV}$. It is still unclear to us what caused the voltage to eventually spike to $\sim 11\text{ V}$, at which point the ion pump was turned off immediately. Once removing the transfer cavity chamber from the optics table and back to the table where the turbo pump sat, we reconnected the turbo pump and did a very quick helium leak test of the transfer cavity system, which is a method that is often used in vacuum work if it is suspected that there is a leak from the assumed vacuum system. The turbo pump at this point in time was connected to a residual gas analyzer (RGA). We took some RGA scans of the partial pressures with respect to different atomic masses as well as some pressure-versus-time scans of specific atomic masses. The results of these scans just verified our decision that the transfer cavity chamber needed to be re-baked.

After baking the cavity vacuum housing at a temperature of $\sim 80^\circ\text{C}$ for another two weeks and then cooling the temperature back down to room temperature, we discovered that the KF-seal connecting the BNC feedthrough to the chamber was loose when we accidentally pumped that area of the chamber when we were trying to get the mini-ion pump started. We observed the pressure of the turbo pump spike when we bumped this region. We also noticed that the transfer cavity vacuum window holders could be tightened closer to the chamber base if we carefully replaced the screws for shorter ones. Luckily, we were able

to replace all the window holder screws for much shorter ones, without breaking vacuum (the pressure of our system remained at around 2.1×10^{-7} mbar!) For future assemblies of the cavity chamber, make sure you have the correct screw lengths for attaching the window holders and/or make the depth of the threaded holes for the window screws deeper.

We were able to get the mini-ion pump started again and be able to regulate itself without the aid of the turbo pump. It is now currently sitting on the optics table and it is fully aligned to the transfer cavity optical setup that will be discussed in Ch. 5 and Ch. 6. The present readings of the ion pump's voltage is ~ 28.85 mV.

3.3 Optical Setup & Detection

The initial layout of the main optical components required to align the reference laser and the three $^{171}\text{Yb}^+$ laser frequencies is displayed below in Fig.3.4. As shown in Fig.3.4, a fiber, one for each laser frequency, is connected to a fiber coupler in order to deliver each frequency to the setup. The other end of each fiber is connected to another fiber coupler, located in a different area of the experiment, in which the initial light stemming from the laser is coupled. The fiber couplers and the photodetectors from left to right are arranged by increasing wavelength.

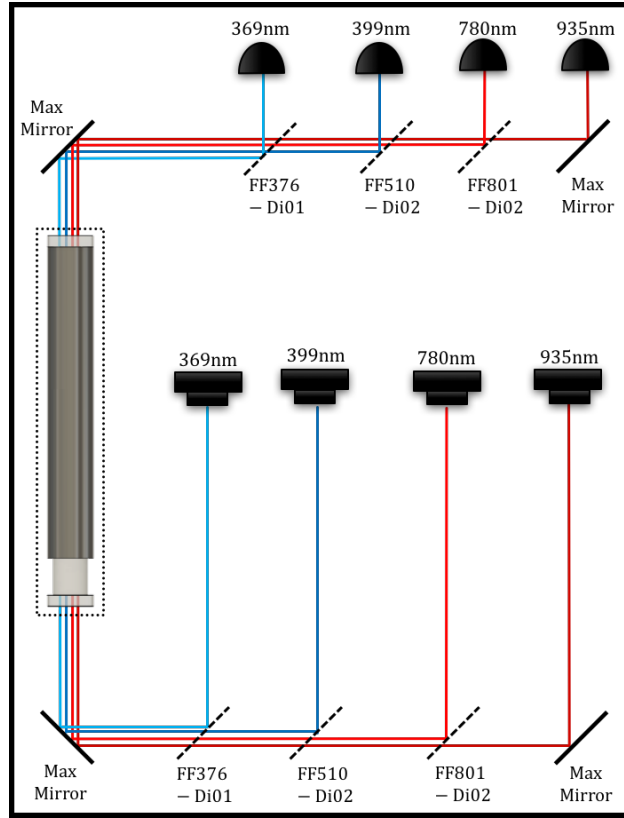


Figure 3.4. Initial Setup of Transfer Cavity System: The main optical elements other than the mode-matching lenses are laid out in the diagram above. These elements include four optical fibers that connect to their own fixed focus fiber collimator, long-pass dichroic filters, broadband mirrors, the transfer cavity of course, and a line of photodetectors.

The transfer cavity is located on the left side of the setup, and the dashed black rectangle around the two mirrors represents the vacuum chamber in which the cavity sits. Surrounding the cavity input and output are a set of broadband dielectric mirrors and long-pass dichroic filters, both from Semrock, that guide the fiber-coupled light to the input (curved-mirror) of the cavity and guide the cavity-coupled output to a row of Thorlabs photodetectors. Not shown in Fig. 3.4 are the coupling lenses that are needed to match the mode of each laser to the supported cavity modes. Ch. 6 discusses these focusing lenses in more detail. The rest of this chapter will discuss the various factors that might impose a limitation to the detection of the four cavity output voltage signals on the chosen photodetectors.

The ability for each photodetector to be able to measure the single laser voltage that it is supposed to detect depends on the gain and responsivity of the detector itself as well as the reflection and transmission coefficients of the long-pass dichroic filters. In addition, the reflectivity of the cavity mirrors (discussed in Ch. 3), the coupling of the lasers to the cavity, and the input power in each laser are other important factors that influence the ability to detect the output laser signals. If we make the assumption that the optical alignment of the entire system is good and the amount of loss in power for each laser at the output of the transfer cavity is about 50 % of the power measured right before the input of the cavity, then we make the argument that only the amount of power in each laser, the reflection and transmission coefficients of the dichroic filters, and the properties of the photodetectors (gain and sensitivity) will then be the primary factors affecting the detection of the cavity-coupled lasers. In addition, we justify that the chosen photodetectors are sufficient for our detection.

The amount of power that can be coupled into each fiber for the transfer cavity setup represents power that is not needed to run our lab's experimental setup. Due to needing more power in the 369 nm and 399 nm lasers than in the 780 nm and 935 nm lasers, the powers coupled into the fibers for the transfer cavity system are significantly higher in the

red wavelengths than in the blue wavelengths. The amount of power in each laser measured at the output of its corresponding fiber coupler, P_{FC} , and the power measured right before the input of the transfer cavity, P_{in} , are displayed in Table 3.1.

Table 3.1. Laser Powers at the Input of the Transfer Cavity

λ	P_{FC}	P_{in}
369 nm	$\sim 35.1 \mu\text{W}$	$\sim 31.3 \mu\text{W}$
399 nm	$\sim 90.5 \mu\text{W}$	$\sim 78.7 \mu\text{W}$
780 nm	$\sim 800 \mu\text{W}$	$\sim 641 \mu\text{W}$
935 nm	$\sim 1.1 \text{ mW}$	$\sim 761 \mu\text{W}$

The differences in laser power presents another factor to consider when choosing the photodetectors to detect the laser signals. In our transfer cavity setup, we have chosen to use Si amplified photodetectors with an adjustable gain from Thorlabs (P/N: PDA36A). [21] These photodetectors are able to detect a broad range of wavelengths (350 nm–1100 nm), including the four in our system; have a low noise-equivalent power range; and have a bandwidth range of up to 10 MHz.

The responsivity of the photodetector is wavelength-dependent while its gain is inversely proportional to the effective bandwidth of the detected signal. The responsivity of these photodetectors is better for the longer wavelengths, which suggests that the gain of photodetectors for 369 nm and 399 nm will need to be higher than for the ones for the 780 nm and 935 nm signals. Table 3.2, on the next page, shows the responsivity of these photodetectors at the four laser wavelengths in our setup. The responsivity data of these detectors was provided by Thorlabs along with other data specifications. [21]

Table 3.2. PDA36A Si Adjustable Gain Photodetector Responsivity

λ	Responsivity
369 nm	$\sim 0.0459 \text{ A/W}$
399 nm	$\sim 0.0612 \text{ A/W}$
780 nm	$\sim 0.478 \text{ A/W}$
935 nm	$\sim 0.615 \text{ A/W}$

The voltage, V_{out} , measured on the photodetector is given by the following equation:

$$V_{\text{out}} = \text{Responsivity} \times \text{Transimpedance Gain} \times \text{Incident Power} \quad (3.8)$$

The long-pass dichroic filters — FF376-Di01, FF510-Di02, and FF801-Di02 — from Semrock were chosen such that the transmission and reflection coefficients for each filter were both as high as possible. All the filters, on average, transmit 93 % of the light in the transmission band and reflect 98 % of the light in the reflection band. The filters were placed in the optical setup to match the order of the fiber couplers and photodetectors as depicted in Fig. 3.4.

Since a difference in power levels exists, we calculated the estimated voltage signal ratios for each photodetector at each wavelength to ensure that these photodetectors would be sufficient for our purpose. Taking into account the fact that the bandwidth of the signal decreases as the gain setting is increased, we used the following gain settings for the photodetectors shown in Table 3.3.

Table 3.3. Photodetector Gain Settings

Photodetector Aligned to	Gain Setting	Transimpedance
369 nm	70 dB	$4.75 \times 10^6 \text{ V/A} \pm 5 \%$
399 nm	60 dB	$1.5 \times 10^6 \text{ V/A} \pm 5 \%$
780 nm	30 dB	$4.75 \times 10^4 \text{ V/A} \pm 2 \%$
935 nm	50 dB	$4.75 \times 10^5 \text{ V/A} \pm 2 \%$

Including the transmission and reflection coefficients for each wavelength in Eq.(3.8), we determined that the 369 nm detector and the 399 nm detector would also measure light from the 780 nm and 935 nm lasers. The 7 % reflectance of 780 nm and 935 nm by the FF376-Di01 and FF510-Di02 filters in addition to the significantly higher power in these wavelengths would drown out the actual voltage signals of the 369 nm and 399 nm wavelengths that their aligned photodetectors would measure. Meanwhile, the 780 nm detector and 935 nm detector are both able to measure their target voltage signals without any significant overlap from the other wavelengths. The calculated voltage ratios for each photodetector is displayed in Table 3.4.

Table 3.4. Voltage Signal Ratios

Photodetector Aligned to	369 nm	399 nm	780 nm	935 nm
369 nm	1	0.137	7.02	12.8
399 nm	8.73×10^{-3}	1	1.77	2.91
780 nm	7.18×10^{-7}	4.63×10^{-5}	1	3.28×10^{-2}
935 nm	1.56×10^{-8}	2.86×10^{-7}	3.42×10^{-3}	1

To minimize the amount of voltage signal due to the longer wavelengths on the 369 nm and 399 nm detectors, we decided to place a FB370-10 bandpass filter on the 369 nm photodetector and a FB400-10 bandpass filter on the 399 nm photodetector, both of which are from Thorlabs. The FB370-10 filter transmits roughly 25 % of the light at 369 nm and has a transmission peak FWHM of 10 ± 2 nm. Similarly, the FB400-10 filter transmits about 25 % of the light at 399 nm and has a transmission peak FWHM of 10 ± 2 nm.

Including these two bandpass filters into the voltage ratio calculations and using the same gain settings, we find that the addition of these two filters is a valid solution. The recalculated voltage ratios are shown on the next page in Table 3.5.

Table 3.5. Voltage Signals Ratios with the Addition of the Two Bandpass Filters

Photodetector Aligned to	369 nm	399 nm	780 nm	935 nm
369 nm	1	2.78×10^{-10}	8.14×10^{-7}	$\times 10^{-4}$
399 nm	1.19×10^{-8}	1	2.78×10^{-8}	2.42×10^{-5}
780 nm	7.18×10^{-7}	4.63×10^{-5}	1	3.28×10^{-2}
935 nm	1.56×10^{-8}	2.86×10^{-7}	3.42×10^{-3}	1

Despite significant differences in power between each of the four lasers and the assumption that the output side of the cavity will only have 50 % of the initial input power, we are able to use the Si adjustable gain photodetectors to detect the voltage signal of the aligned target wavelength. The addition of the two bandpass filters, one on the 369 nm detector and the other on the 399 nm detector to the optical setup shown in Fig. 3.4, significantly blocks any reflected 780 nm or 935 nm voltage signals on those detectors.

3.4 Coupling Optics for Mode-Matching

Before determining the coupling optics for mode-matching each wavelength to the transfer cavity, we will briefly discuss the Gaussian-type modes of an optical resonator. In solving the paraxial wave equation for the propagation of light traveling in the z-direction (parallel to the optical axis of the cavity) through an optical resonator composed of two mirrors separated by a distance L, one finds that the longitudinal waves of the optical cavity are standing waves while the transverse spatial modes of the cavity are Hermite-Gaussian (HG) TEM_{lm} modes (normalized in Cartesian coordinates [23]):

$$E_{lm}^{(HG)}(x, y, z) = E_0 \frac{w_0}{w} \sqrt{\frac{1}{2^{l+m} l! m!}} H_l \left[\frac{x\sqrt{2}}{w} \right] H_m \left[\frac{y\sqrt{2}}{w} \right] \exp \left[\frac{-(x^2 + y^2)}{w^2} \right] \times \exp \left[i \left(\frac{k(x^2 + y^2)}{2R} + kz - (l + m + 1)\psi \right) \right] \quad (3.9)$$

or Laguerre-Gaussian (LG) TEM_{lm} modes (normalized in Cylindrical coordinates [23]):

$$E_{lm}^{(LG)}(\rho, \phi, z) = E_0 \frac{w_0}{w} \sqrt{\frac{2l!}{\pi(l + |m|)!}} L_l^{|m|} \left[\frac{2\rho^2}{w^2} \right] \left(\frac{\rho\sqrt{2}}{w} \right)^{|m|} \exp \left[\frac{-\rho^2}{w^2} \right] \times \exp \left[i \left(\frac{k\rho^2}{2R} + kz + m\phi - (2l + |m| + 1)\psi \right) \right] \quad (3.10)$$

The fundamental mode of the cavity, in general, is the Gaussian TEM₀₀ mode in which the indices l and m are both zero. [23] In Eq.(3.9), Eq.(3.10), E₀ is an amplitude constant, k is the wavenumber (k=2π/λ), w₀ is the characteristic Gaussian beam waist:

$$w_0 = \sqrt{\frac{\lambda z_R}{\pi}}; \quad (3.11)$$

w is the width of the Gaussian beam as a function of position z with respect to the beam waist position at $z = 0$:

$$w(z) = w_0 \sqrt{1 + \left(\frac{z}{z_R}\right)^2}; \quad (3.12)$$

R is the radius of curvature of the Gaussian wavefront as a function of position z :

$$R(z) = z \left[1 + \left(\frac{z_R}{z}\right)^2 \right]; \quad (3.13)$$

and ψ is known as the Gouy phase of the propagating beam at position z :

$$\psi(z) = \tan^{-1}\left(\frac{z}{z_R}\right) \quad (3.14)$$

The parameter z_R is the Rayleigh range which defines the distance from the beam waist w_0 , where the beam width w is increased by a factor of $\sqrt{2}$ and is generally defined by rearranging Eq.(3.11). However, z_R can also be obtained by rearranging Eq.(3.13) or Eq.(3.12) in terms of either the radius of curvature or the beam width at position z . For a hemi-confocal cavity, such as ours, the Rayleigh range can be expressed by the radius of curvature of the concave mirror, R_1 , and the length of the cavity, L , by rearranging Eq.(3.13) as follows:

$$z_R = \sqrt{L(R_1 - L)} \quad (3.15)$$

Since the design of our transfer cavity is hemi-confocal, as discussed in Ch. 3, the Gaussian beam width at the front face of the plane mirror ($z = 0$) will be the location of the beam waist and the radius of curvature of wavefront at the plane mirror is infinite. The Gaussian beam at the curved mirror face will have a wavefront curvature that matches the radius of curvature of the concave mirror, $R = 600$ mm, and the beam width at this location, $z = L = 190.815$ mm, can be calculated using equation Eq.(3.12). These beam widths of the transfer cavity are depicted in Fig. 3.5.

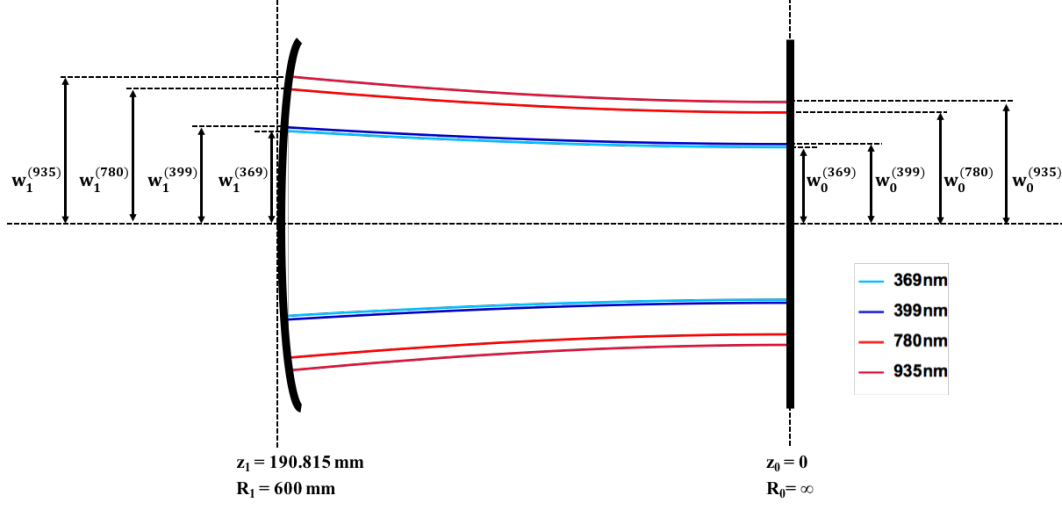


Figure 3.5. Gaussian Beam Widths of Transfer Cavity: The widths of the propagating beams are displayed for all four wavelengths at the location of the curved mirror and at the location of the plane mirror.

To determine how much the laser beam width at the output of the fiber coupler laser beam must change in order to match the beam waist, we first used Eq.(3.15) to obtain the Rayleigh range of our cavity ($z_R \sim 280$ mm) to substitute it into Eq.(3.11) to calculate the beam waist for each wavelength. Then we made the assumption that the width of the beam from the output of the fiber coupler would be collimated and would have a width of one-half of the beam diameter as specified by the optical properties of that fiber coupler. Finally, we calculated the ratio between the fiber coupler output beam width, w_{FC} , and the Gaussian beam waist, w_0 . Table 3.6 displays the w_0 , w_{FC} , and the ratio between the two widths for each wavelength that we will mode-match to the cavity.

Table 3.6. Mode-Matching Beam Widths

λ	w_0	w_{FC}	$\frac{w_{FC}}{w_0}$
369 nm	0.1812 mm	0.3150 mm	1.7388
399 nm	0.1884 mm	0.3150 mm	1.6721
780 nm	0.2634 mm	0.4900 mm	1.8603
935 nm	0.2884 mm	0.8700 mm	3.0169

A system of lenses can be used to transform a laser's beam parameters to match the beam parameters of another optical system even though the mode of the beam remains unchanged. [24] We decided to use a telescope system, shown below in Fig. 3.6, to mode-match the two beam widths for each wavelength.

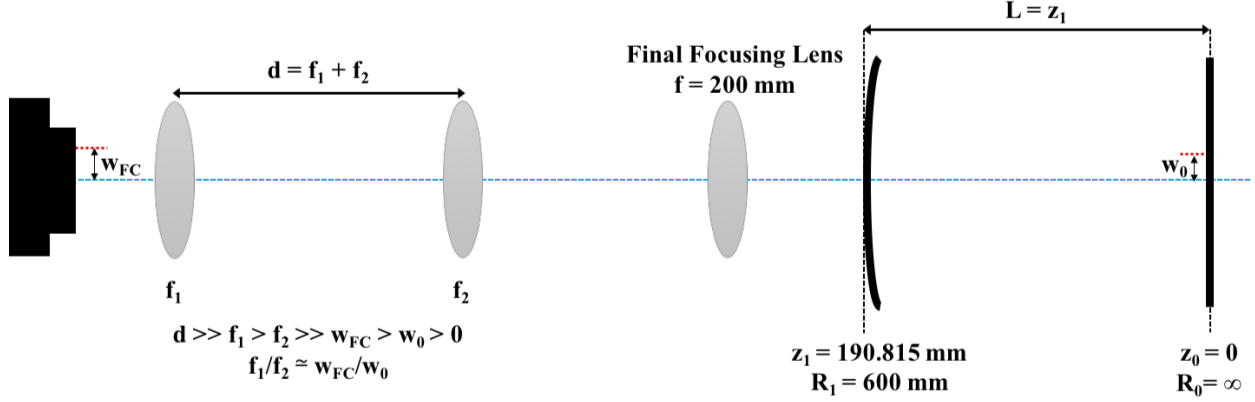


Figure 3.6. Telescope Mode-Matching Coupling Optics

As shown in Fig. 3.6, the length of the telescope for each wavelength will be constrained to fit in the space between the fiber coupler and the dichroic (or mirror for the 935nm path) shown in Fig. 3.4. In addition, the ratio between f_1 and f_2 will need to equal the ratio between w_{FC} and w_0 . Also, the focal lengths f_1 and f_2 were constrained to be an available plano-convex UV-fused silica lens offered by Thorlabs. UV-fused silica glass lenses were chosen since the transmission percentage of light at the wavelengths of 369 nm, 399 nm, 780 nm, and 935 nm is greater than the alternative option of N-BK7 lenses. Using Mathematica to generate matrices of the ratio between available focal lengths and the ratio between the focal length and the effective focal length of a combination of two lenses, Table 3.7 displays the focal lengths of the telescope lenses for each wavelength, the length between the two lenses, the ratio between the two focal lengths, and the ratio of the beam widths that needed to be matched.

Table 3.7. Focal Lengths of Mode-Matching Coupling Optics

λ	f_1	f_2	$d = f_1 + f_2$	$\frac{f_1}{f_2}$	$\frac{w_{FC}}{w_0}$
369 nm	100 mm	~ 57.7 mm	157.7 mm ($\sim 6.2084''$)	1.7333	1.7388
399 nm	125 mm	75 mm	200 mm ($\sim 7.8740''$)	1.6667	1.6721
780 nm	150 mm	~ 80.8 mm	230.8 mm ($\sim 9.0854''$)	1.8571	1.8603
935 nm	150 mm	50 mm	200 mm ($\sim .8740''$)	3.000	3.0169

The mode-matching telescope for the 369 nm and 780 nm laser both have a combination of two lenses to obtain the effective focal length of the second lens. The 369 nm f_2 is achieved by using lenses with focal lengths of 75 mm and 250 mm while the 780 nm f_2 is obtained from using lenses with focal lengths of 150 mm and 175 mm. In addition, the 200 mm focusing lens shown in Fig. 3.6 is A-coated which is best for transmitting the 369 nm light especially since this laser has the lowest amount of power in the transfer cavity system. Some power may be lost in the transmitted light at the other wavelengths, which has been included in our detection calculations discussed in Ch. 5. Finally, with the coupling optics determined, the use of a 50/50 beam-splitter and an Allied Vision Guppy camera are utilized to see the mode structure of each of the lasers to ensure that the TEM₀₀ mode is achieved. Fig. 3.7 represents the complete transfer cavity optical system and shows the addition of UV-fused silica 100 mm focal length plano-convex lenses to all four photodetectors to help focus the output cavity-coupled signals for maximum detection. A complete list of the components used in the final optical setup can be found in Appendix A.

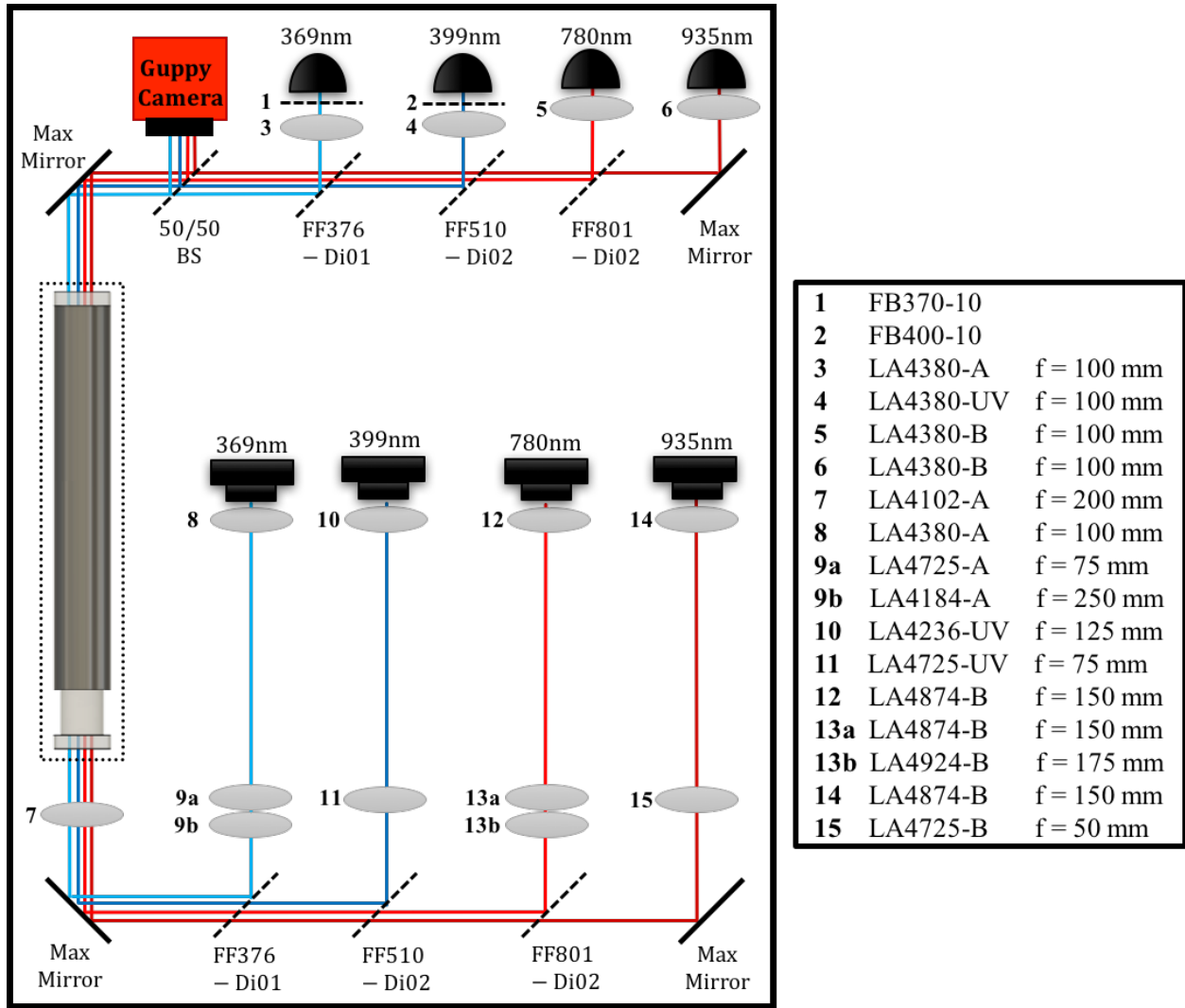


Figure 3.7. Final Optical Setup of Transfer Cavity System

4 Measurements & Results

At the moment, our frequency lock has only been set up and tested to lock only one $^{171}\text{Yb}^+$ CW laser frequency relative to the stabilized reference frequency. We are currently in the process of implementing the software to lock all three laser frequencies simultaneously. However, we present data showing the current status of the transfer cavity lock and its ability to lock the frequency of the 369 nm laser. The transfer cavity locked-laser data points are compared to the results of the same experiment in which the 369 nm laser is now locked to the wavemeter. In these measurements, both the 399 nm and 935 nm lasers are locked by the wavemeter. The goal of these initial measurements is to determine whether our expectation that the overall short-term stability of the transfer cavity frequency lock is similar to the behavior of the wavemeter lock and that the frequency fluctuations about the set point of the locked frequency are more controlled. We wish to observe that the data taken with the transfer cavity lock is less sensitive to the ambient room environments since we placed the transfer cavity under vacuum.

Before we discuss the measurements that were taken, we will briefly mention the beam path of the 369 nm laser in our experiment as a whole. From the 369 nm external cavity laser diode head, the laser light is split into two main paths. The first path is split into two arms in which the 369 nm laser is fiber-coupled into a fiber sent to the wavemeter and into another fiber that is sent to the transfer cavity setup. The second path from the laser head is also split into two additional beam paths that we call cooling and detecting. Both of these beam paths include an electro-optic modulator (EOM), followed by a double-passed acousto-optic modulator (AOM). These two additional beam paths are then recombined and fiber-coupled to a fiber sent to the vacuum chamber containing the ion trap.

In our experimental setup, we use a multi-channel photomultiplier tube (PMT) to collect the scattered photons from the trapped ions. By adjusting the trap potential, we can arrange the spacing between a chain of ions such that the ion fluorescence of each ion can be measured on its own PMT channel. However, for the measurements presented in this senior thesis, we will only be trapping a single ion, and thus only one channel of the PMT will be used to detect the scattered photons. The units of the PMT measurements are in kilo-counts per second (kCounts/s). We initially took a calibration measurement (see Fig. 4.1) of the observed fluorescence counts after cooling the ion for a fixed amount of time as a function of the cooling beam frequency by adjusting the radio frequency (RF) voltage applied to the AOM in the cooling beam path discussed above.

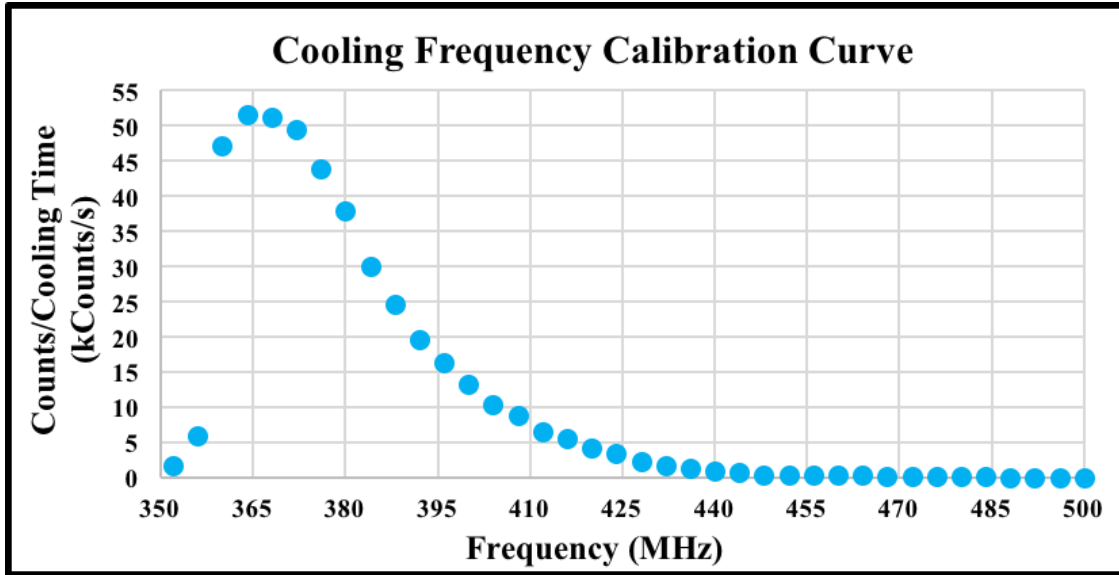


Figure 4.1. Cooling Frequency Calibration Curve

For our ion fluorescence measurements, we decided to set the frequency of the cooling AOM such that the observed counts per second was about half of the maximum counts per cooling time of the calibration curve. Further discussion regarding the use of this cooling frequency calibration curve to convert the ion fluorescence in kCounts/s to a relative frequency in MHz will be discussed after we present the ion fluorescence data for the 369 nm laser stabilized using two different frequency locks.

Next, measured the fluorescence of a single trapped $^{171}\text{Yb}^+$ atom, shown below in Fig. 4.2, with the 369 nm laser locked via the transfer cavity frequency lock and with its frequency stabilized by the wavemeter lock.

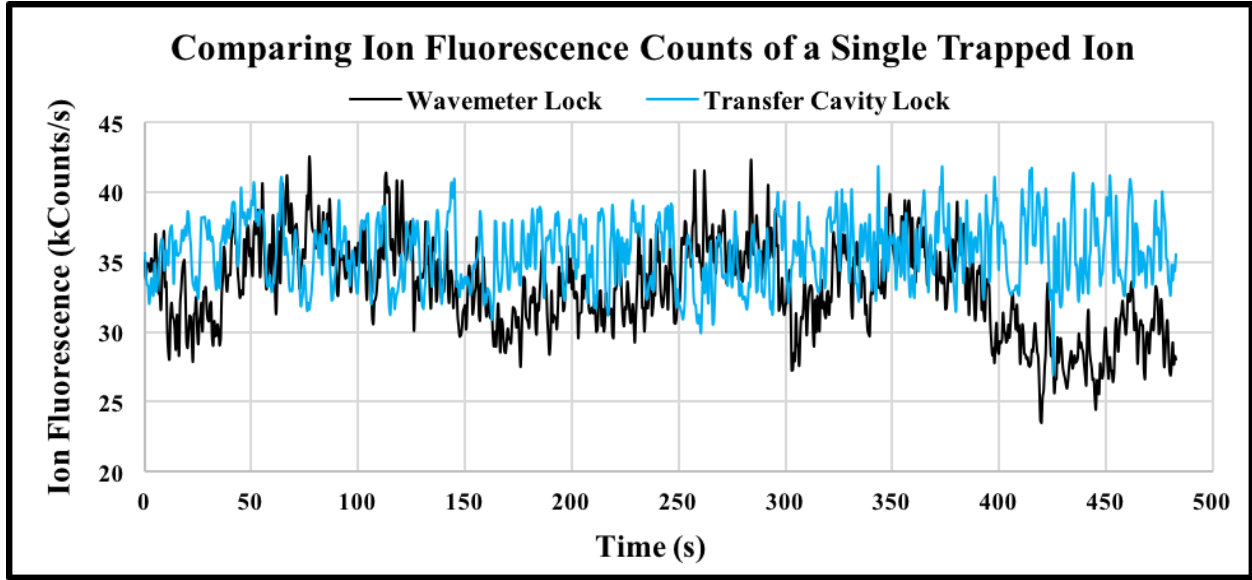


Figure 4.2. Measured Ion Fluorescence using Different Frequency Locks

As shown in Fig. 4.2, the two sets of data are similar in their overall ability to lock and stabilize the set point frequency value of the 369 nm laser since the majority of the counts are measured within the range of 25 kCounts/s to 43 kCounts/s. Also, if either lock was unable to stabilize the frequency relative to the set-point, we would have observed a significant decrease in the counts or a drift in the number of counts in a particular direction. In addition, the transfer cavity locked 369 nm laser frequency data set (the blue trace in Fig. 4.2) has a smaller or more confined deviation away from its average kCounts/s while the wavemeter locked 369 nm laser fluorescence counts have deviations that follow more of a pattern. The pattern of the wavemeter lock count fluctuations (the black trace in Fig. 4.2) seem to continue slightly longer in one direction before the direction changes, such as from 125 s to 175 s with a negative slope and from 175 s to 250 s with a positive slope.

These qualitative observations of the ion fluorescence counts are confirmed by the mean, standard deviation, and variance for each frequency lock measurement. The mean ion fluorescence measured for the 369 nm laser locked via the transfer cavity frequency lock is 35.7 ± 0.1 kCounts/s. The mean ion fluorescence of the wavemeter locked 369 nm laser data is 33.1 ± 0.1 kCounts/s. The associated errors in the mean fluorescence only represent the statistical uncertainty in the mean value and do not account for any systematic errors or other sources that would affect the uncertainty in the mean. These mean fluorescence values are also listed in Table 4.1, which also gives the calculated values of the standard deviation and variance in the fluorescence counts.

Table 4.1. Mean, Standard Deviation, & Variance in Ion Fluorescence Data Sets

Ion Fluorescence Data with	Mean	Standard Deviation	Variance
Transfer Cavity Lock	35.7 ± 0.1 kCounts/s	± 2.3 kCounts/s	$5.4 \text{ (kCounts/s)}^2$
Wavemeter Lock	33.3 ± 0.1 kCounts/s	± 3.3 kCounts/s	$10.7 \text{ (kCounts/s)}^2$

The deviation and variance of the measured fluorescence counts with the 369 nm laser frequency locked by the transfer cavity lock are indeed smaller than the deviation and variance of the ion counts measured with the frequency 369 nm laser. We did not focus on quantifying the errors associated with other parts of the experiment that would affect the ion fluorescence counts since our goal with taking these measurements was to demonstrate a proof-of-principle result, that our transfer cavity setup (hardware and current status of the software) works. We know that parts of the transfer cavity system need to be optimized, and we will discuss these areas in Ch. 8.

Next, we used the cooling frequency calibration curve, Fig. 4.1, to extract a relationship between the units of kCounts/s and MHz. We fit the data points located on the side of the calibration peak spanning the range of kCounts/s that we observed in the ion fluorescence measurements.

We approximated that the units of kCounts/s and the units of MHz were linearly proportional to each other for these set of points. We used the following fit equation,

$$y = m x + b \quad (4.1)$$

where m is the slope of the line and b is the y-intercept. Fig. 4.3 displays the linear fit for the four data points in the range of ~ 20 – 45 kCounts/s.

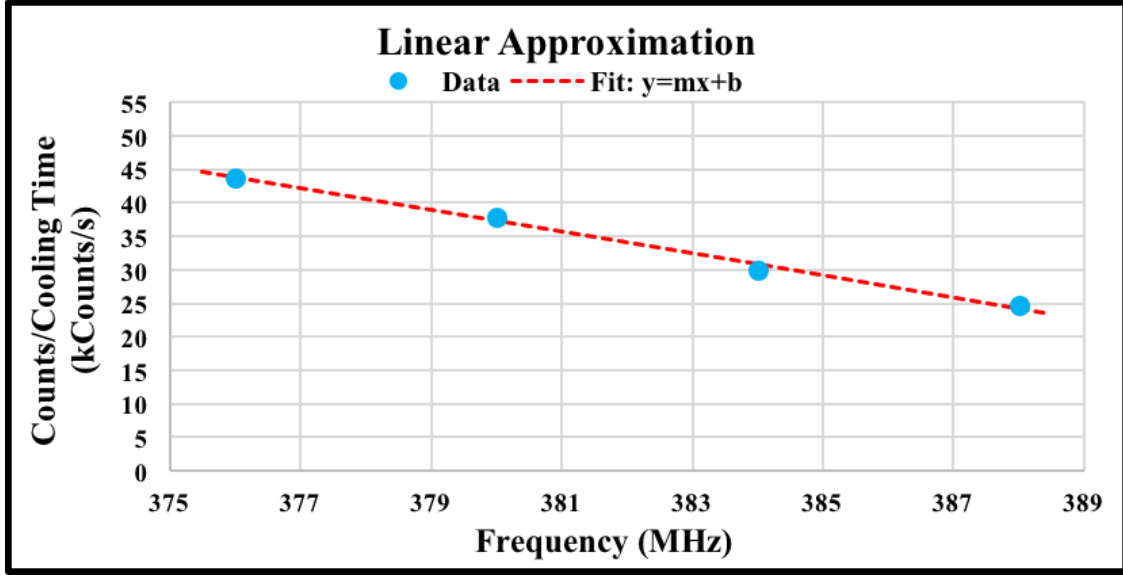


Figure 4.3. Linear Fit

The fit parameters and associated uncertainties are displayed in Table 4.2. Table 4.2 also shows the P-value for the linear fit of the data, a value indicating an agreement of about 36.8 %.

Table 4.2. Linear Fit Parameters for “Converting from MHz to kCounts/s”

Slope m	y-Intercept b	P-value
-1.633 ± 0.086	658 ± 33	$0.368 = 36.8 \%$

The uncertainties for the slope and y-intercept shown in Table 4.2 are obtained by using the error-propagation equations found in Taylor’s *An Introduction to Error Analysis*. [25]

Using the fit parameter values and rearranging Eq.(4.1) we can obtain a function of frequency in MHz in terms of the measured ion fluorescence in kCounts/s:

$$x = \frac{y - b}{m} \quad (4.2)$$

where m is the slope and b is the y-intercept of the linear fit in Eq.(4.1). Finally, using this conversion relation, Eq.(4.2) to translate from units of kCounts/s to units of MHz, we can translate the ion fluorescence measurements taken for the two different locking methods of the 369 nm laser frequency to obtain the frequency of the cooling beam AOM. Then, a relative frequency measurement of the 369 nm laser can be achieved by using the frequency values of the AOM which are displayed in Fig. 4.4.

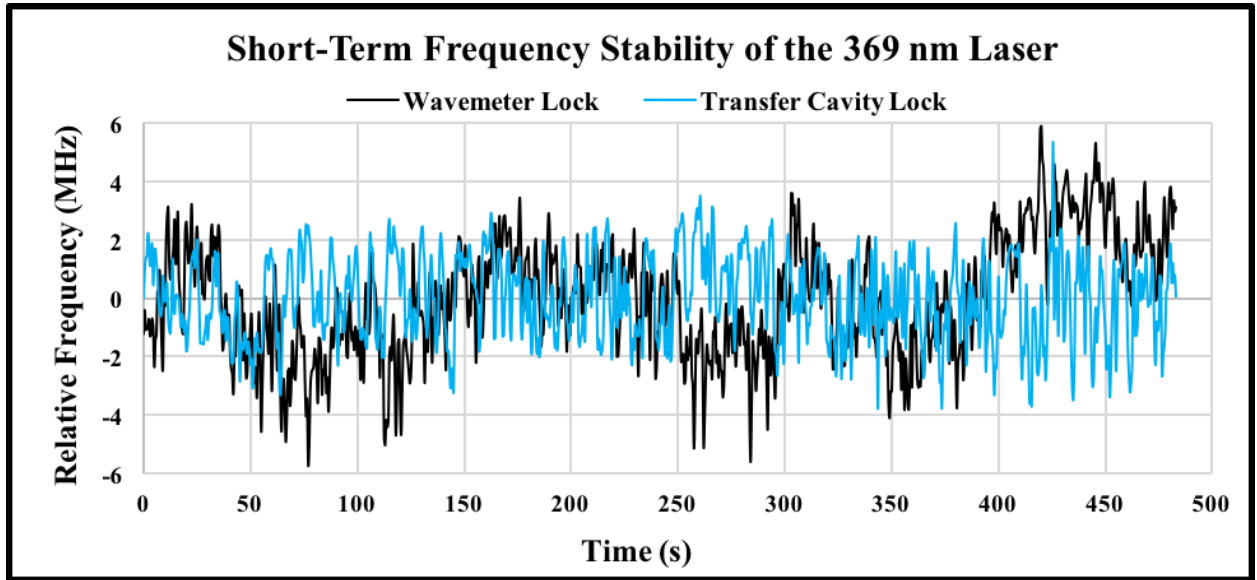


Figure 4.4. 369 nm Laser Short Term Frequency Stability

In Fig. 4.4, we see the same results that we made and discussed regarding the ion fluorescence data. Also, for short time scales (~ 8.1 minutes), the relative frequency deviation of the lock point of the 369 nm laser is ± 1.4 MHz while the deviation of the laser lock point using

the wavemeter lock is ± 2.0 MHz. Table 4.3 shows these standard deviations as well as the variance for the relative frequency data of the locked 369 nm laser using the transfer cavity lock and the wavemeter lock.

Table 4.3. Relative Frequency Stability of the 369 nm Laser Standard Deviation & Variance

369 nm Laser Locked via	Standard Deviation	Variance
Transfer Cavity Lock	± 1.4 MHz	2.0 (MHz)^2
Wavemeter Lock	± 2.0 MHz	4.0 (MHz)^2

This initial comparison of the performance of the transfer cavity lock with the wavemeter lock done by measuring the ion fluorescence and converting it into a measurement of the relative frequency of the 369 nm laser confirmed for us that our expectations about the first initial measurements of the transfer cavity were correct. In addition, the short-term measurement in which the 369 nm laser was locked by the transfer cavity had fewer irregular fluctuations about the mean (a less noisy signal) than the data taken with only the wavemeter locking the frequencies of the lasers. This result suggests that the evacuated transfer cavity is not directly influenced by any noise or changes in the ambient environment of the lab. We also looked at the wavemeter readings of the frequency value of the 369 nm laser during both fluorescence measurements. However, no new information about the performance of the transfer cavity lock could be gained, such as whether one frequency locking method performed better than the other. Overall, these first sets of data that were taken using the transfer cavity to lock the 369 nm laser seem promising in terms of the long-term performance of the frequency stability since we have not even begun optimizing parts of the transfer cavity system that we have already identified as needing improvement.

5 Discussion & Conclusion

We are in the initial stages of implementing a transfer cavity system. The system's hardware which is composed of the physical transfer cavity, vacuum housing, and optical alignment are all in place while the software-side of the system (the frequency lock and feedback) are currently being coded. However, we have presented preliminary measurements of the ion fluorescence PMT counts of a single trapped ion in which the 369 nm laser frequency was being locked and stabilized by the transfer cavity in reference to the stabilized 780 nm laser while the frequencies of the 399 nm and 935 nm lasers were still being locked using the wavemeter. These initial sets of data are quite promising since we observe a smaller variance from the 369 nm frequency locked value when the that laser is stabilized by the transfer cavity system than when it is locked by the wavemeter.

A complete characterization of our transfer cavity system and its ability to minimize long-term frequency drifts cannot be extracted from these short-term measurements. So our first goal is to finish implementing the FPGA-controlled frequency lock code such that all three $^{171}\text{Yb}^+$ lasers can be locked and receive feedback in order to keep each of their calculated α values (Eq.(2.1)) constant with the initially chosen alpha-values (α_0). Then, we plan on measuring the ion fluorescence PMT counts of a single ion with all three lasers locked via the transfer cavity. From this much longer set of data, we can characterize how well we can stabilize our 369 nm and 935 nm laser frequencies in terms of their corresponding linewidths. A measurement of any long-term frequency drift can also be obtained as well by taking an Allen variance. [26, 27]

In general, further optimization can be done in both the hardware and software setups that will likely improve the performance of the transfer cavity frequency stability lock. One of the parameters that is limiting the ability of the frequency lock is how fast we are able to scan

the length of the cavity which is controlled by the triangular ramp frequency that is amplified by the HV amplifier to drive the cylindrical piezo tube. The fluorescence measurements were taken with a piezo ramp at 5 Hz which is extremely slow. We would like to be able to drive the piezo at 100 Hz, but significant differences in the 369 nm laser's power in comparison to the longer wavelengths means that the photodetector measuring the 369 nm cavity output signal has to be on its highest gain setting (70 dB). A larger gain is proportional to a smaller bandwidth that the photodetector can measure, and so a faster scan rate with our current setup will mean that it will be unable to detect the resonant transmission peaks of the 369 nm laser since the amplitude of this laser is significantly smaller than the other three lasers. The powers of each of the lasers measured in front of the photodetectors can easily be increased by a factor of two by removing the 50/50 beamsplitter that splits the output cavity-coupled laser signals between backline of photodetectors and the guppy-camera used to look at the resonant spatial modes of each of the lasers and some slight re-alignment of the output cavity turning mirror and dichroic filters. With double the amount of power at the 369 nm and 399 nm photodetectors, hopefully the bandwidth can be increased by being able to turn down the gain by 10 dB. Also, we can use other photodetectors that are more sensitive to the bluer wavelengths and that also have a better bandwidth. Increasing the photodetector bandwidths will allow us to increase the scan rate from the slow sweep of 5 Hz which will improve the speed and performance of the frequency lock.

In addition, the software implementation of the transfer cavity frequency locking system can be optimized by improving the determination of the transmission peak times and by dividing down the linewidth. A better determination of the initial alpha value and subsequent alpha values that will be compared to the chosen value can be obtained by using a larger sample of data points to determine the maximum peak which has already been optimized to belong to the TEM₀₀ mode with the other frequency transmission peaks significantly smaller in

amplitude. Software optimization can also be obtained from improving the feedback of the error signals to the laser controller as well as coming up with a way to send feedback to the SRS function generator that produces the triangle ramp driving the piezo of the cavity.

At this moment, it is not possible to determine whether our transfer cavity frequency stabilization system will completely replace the current wavemeter lock. However, based on the observed reduction of fluctuations of the locked 369 nm laser frequency away from the locking point in comparison to the wavemeter lock, the use of the transfer cavity lock for the 369 nm laser could potentially improve our ability to cool and detect $^{171}\text{Yb}^+$ ions in our experiments.

Appendix A Lists of Components

A.1 Lasers & Wavemeter

- 369 nm Laser
- 399 nm Laser
- 935 nm Laser
- 780 nm Laser
- HighFinesse Wavemeter

A.2 Transfer Cavity

- Transfer Cavity Mirrors (*Lambda Research Optics Inc.*)
- Transfer Cavity Assembly Jigs
- INVAR Rod
- Piezoelectric Cylindrical Tube (*American Piezo International, Ltd.*)
- Torr Seal
- UHV-compatible Butane Soldering Iron (*Accu-Glass Products, Inc.*)
- UHV In-Vacuum Solder (*Accu-Glass Products, Inc.*)
- UHV Copper Enamel Wire, 34 AWG
- And Patience!

A.3 KF Vacuum Chamber

- Mini-Ion Pump
- MiniVac Controller

- KF-16 Angle Valve
- KF Vacuum Base & Lid
- KF-16 & KF40 Vacuum Pieces
- Thorlabs Windows (P/N: WG41050)
- Window Chamber Holders
- Correct size screws
- Kapton Tape
- Thermal Coupler
- Pfeiffer Turbo Pump

A.4 Complete Optical Setup

Company	Part Number	Quantity	Component
Semrock	FF376-Di01-25x36	2	376 nm edge BrightLine single-edge dichroic beamsplitter
" "	FF510-Di02-25x36	2	510 nm edge BrightLine single-edge dichroic beamsplitter
" "	FF801-Di02-25x36	2	801 nm edge BrightLine single-edge dichroic beamsplitter
" "	MM3-311S-t6-25	4	350 - 1100 nm MaxMirror ultra-broadband mirror
Thorlabs	FB370-10	1	1" Bandpass Filter, CWL = 370 2 nm, FWHM = 10 2 nm
" "	FB400-10	1	1" Bandpass Filter, CWL = 400 2 nm, FWHM = 10 2 nm
" "	BSW26	1	1" 50:50 UVFS Plate Beamsplitter, Coating: 350 - 1100 nm, t = 5 mm
" "	F671APC-405	2	405 nm, f=4.02 mm, NA=0.60 FC/APC Fiber Collimation Pkg.
" "	F230APC-780	1	780 nm, f = 4.51 mm, NA = 0.55 FC/APC Fiber Collimation Pkg.
" "	F240APC-850	1	850 nm, f = 8.02 mm, NA = 0.50 FC/APC Fiber Collimation Pkg.
" "	SM300-CUSTOM	2	Custom Patch Cable - Fiber: SM300,Tubing: FT900Y, End 1: FC/PC, End 2: FC/APC, Length: 3 m
" "	780HP-CUSTOM	2	Custom Patch Cable - Fiber: 780HP, Tubing: FT900Y, End 1: FC/PC, End 2: FC/APC, Length: 3 m
" "	PDA36A	4	Si Switchable Gain Detector, 350-1100 nm, 10 MHz BW, 13 mm2, 8-32 Taps
" "	AD11F	1	SM1-Threaded Adapter for 11 mm Cylindrical Components
" "	AD12F	3	SM1-Threaded Adapter for 12 mm Cylindrical Components
" "	KM100	2	Kinematic Mirror Mount for 1" Optics
" "	KC1-T	4	Kinematic, SM1-Threaded, 30 mm-Cage-Compatible Mount for 1" Optic
" "	LMR1	4	Lens Mount with Retaining Ring for 1" Optics, 8-32 Tap
" "	KM100S	8	Kinematic Mount for 1" (25.4 mm) Tall Rectangular Optics, Right Handed
" "	TR1.5		1/2" Optical Post, SS, 8-32 Setscrew, 1/4"-20 Tap, L = 1.5"
" "	TR2		1/2" Optical Post, SS, 8-32 Setscrew, 1/4"-20 Tap, L = 2"
" "	PH1.5		1/2" Post Holder, Spring-Loaded Hex-Locking Thumbscrew, L = 1.5"
" "	PH2		1/2" Post Holder, Spring-Loaded Hex-Locking Thumbscrew, L = 2"
" "	BE1		1.25" Studded Pedestal Base Adapter, 1/4"-20 Thread
" "	CF125		Clamping Fork, 1.24" Counterbored Slot, Universal
" "	SMIRC	8	1.20" Slip Ring for SM1 Lens Tubes, 8-32 Tap
" "	SM1V10	4	1" Adjustable Lens Tube, 0.81" Travel Range
" "	SM1L03	12	SM1 Lens Tube, 0.30" Thread Depth, One Retaining Ring Included
" "	SM1L05	6	SM1 Lens Tube, 0.50" Thread Depth, One Retaining Ring Included
" "	SM1L10	8	SM1 Lens Tube, 1.00" Thread Depth, One Retaining Ring Included
" "	SM1M20	2	SM1 Lens Tube Without External Threads, 2" Long, Two Retaining Rings Included
" "	SM1M30	3	SM1 Lens Tube Without External Threads, 3" Long, Two Retaining Rings Included
" "	LA4725-A	1	f=75 mm, 1" UVFS Plano-Convex Lens, ARC: 350 - 700 nm
" "	LA4380-A	2	f=100 mm, 1" UVFS Plano-Convex Lens, ARC: 350 - 700 nm
" "	LA4102-A	1	f=200 mm, 1" UVFS Plano-Convex Lens, ARC: 350 - 700 nm
" "	LA4158-A	1	f=250 mm, 1" UVFS Plano-Convex Lens, ARC: 350 - 700 nm
" "	LA4725-UV	1	f = 75.0 mm, 1" UV Fused Silica Plano-Convex Lens, AR Coating: 245-400 nm
" "	LA4380-UV	1	f = 100.0 mm, 1" UV Fused Silica Plano-Convex Lens, AR Coating: 245-400 nm
" "	LA4236-UV	1	f = 125.0 mm, 1" UV Fused Silica Plano-Convex Lens, AR Coating: 245-400 nm
" "	LA4380-B	2	f=100 mm, 1" UVFS Plano-Convex Lens, ARC: 650 - 1050 nm
" "	LA4148-B	1	f=50 mm, 1" UVFS Plano-Convex Lens, ARC: 650 - 1050 nm
" "	LA4874-B	2	f=150 mm, 1" UVFS Plano-Convex Lens, ARC: 650 - 1050 nm
" "	LA4924-B	1	f=175 mm, 1" UVFS Plano-Convex Lens, ARC: 650 - 1050 nm

Appendix B Diagrams & Drawings

B.1 Ytterbium-171 Energy Diagram

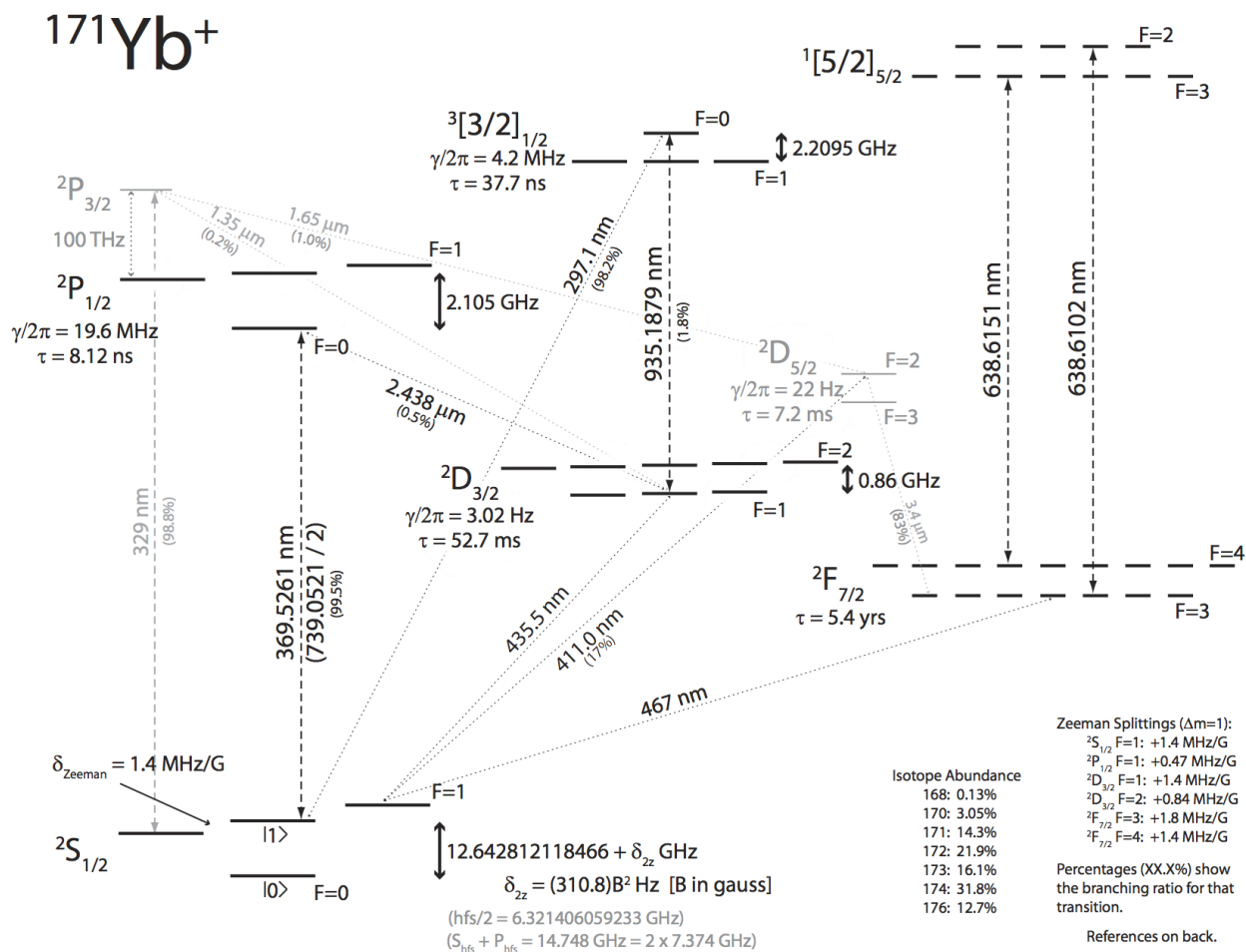


Figure B.1. Detailed $^{171}\text{Yb}^+$ Energy Level Diagram

Invar Cavity
 July 7, 2009
 Material: Invar 36 (provided)
 Quantity: 10
 Tolerance: X.XXX --> 0.005%
 X.XX --> 0.01%
 Contact: Jonathan Mizrahi

DRAWN	monroe-lab	7/7/2009	TITLE	
CHECKED				
QA				
RFQ				
APPROVED				
			SIZE	CWG NO
			C	InvarCavity
			SCALE	REV

SHEET 1 OF 1

44

B.3 Transfer Cavity Assembly Jigs

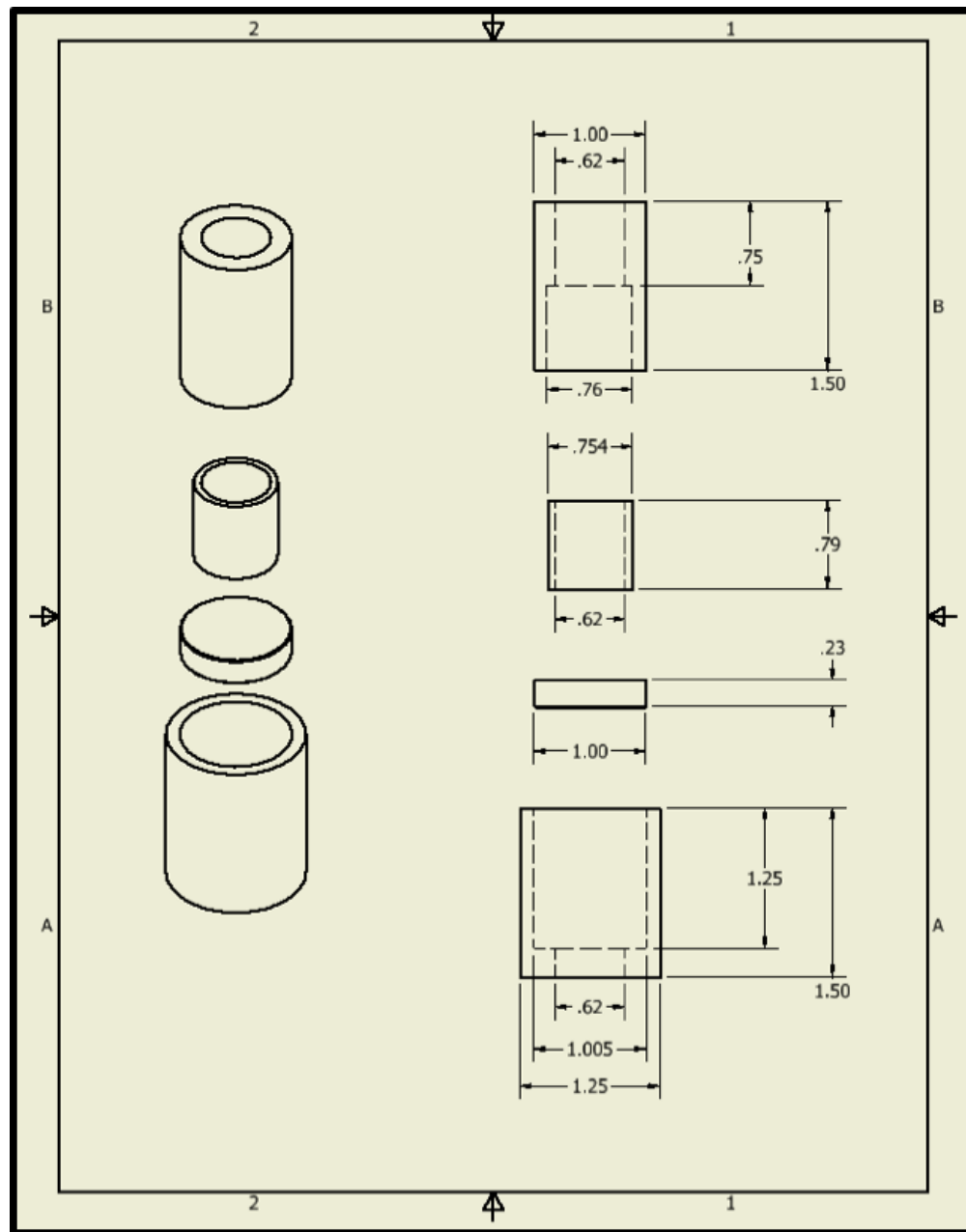


Figure B.3. Transfer Cavity Assembly Jigs: The dimensions of the mirror jig and piezo jig are shown in this drawing. In addition, the drawing includes the pictures of the mirror and the piezo to demonstrate how the jigs are used.

B.4 Vacuum Window Holders

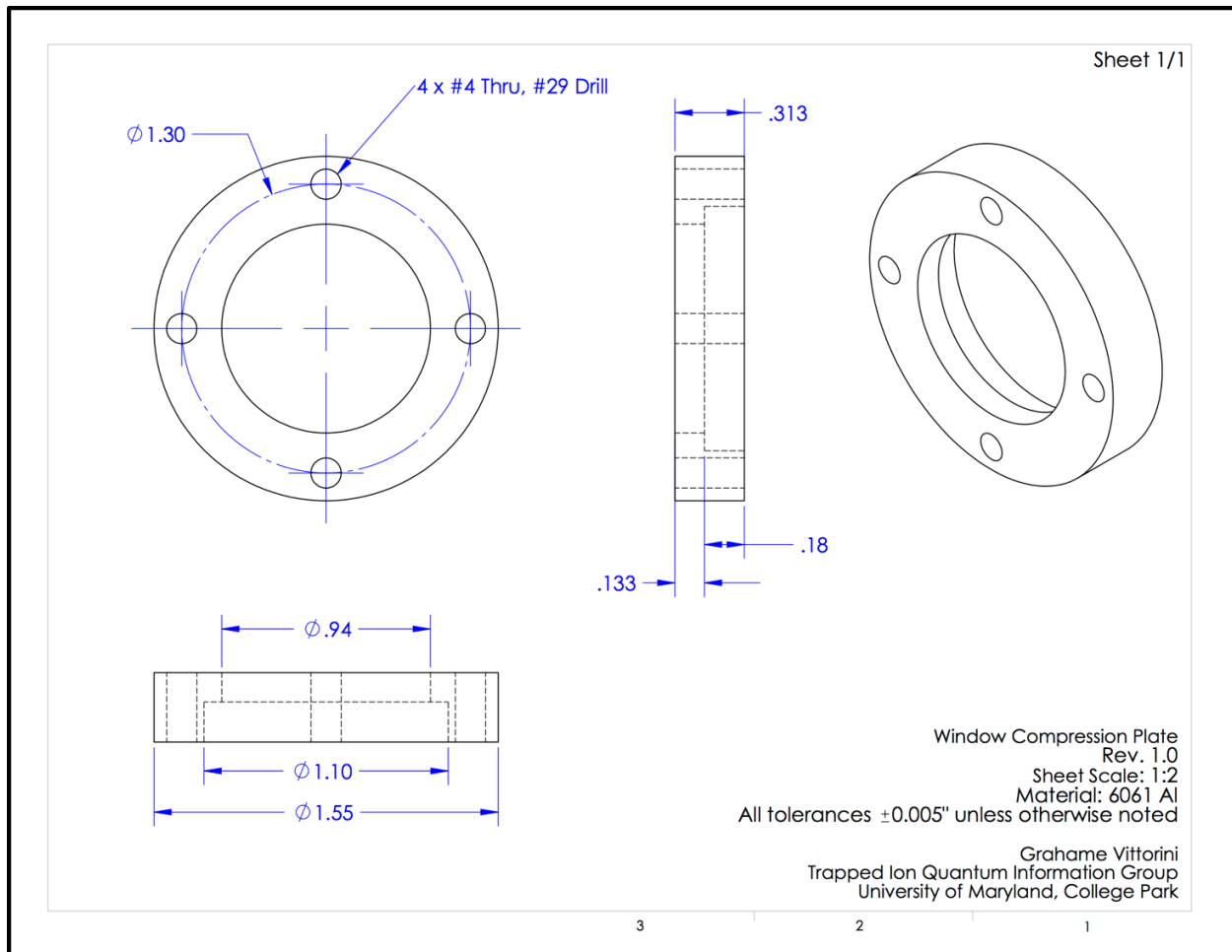


Figure B.4. Transfer Cavity Chamber Window Holders

B.5 KF Vacuum Chamber Base

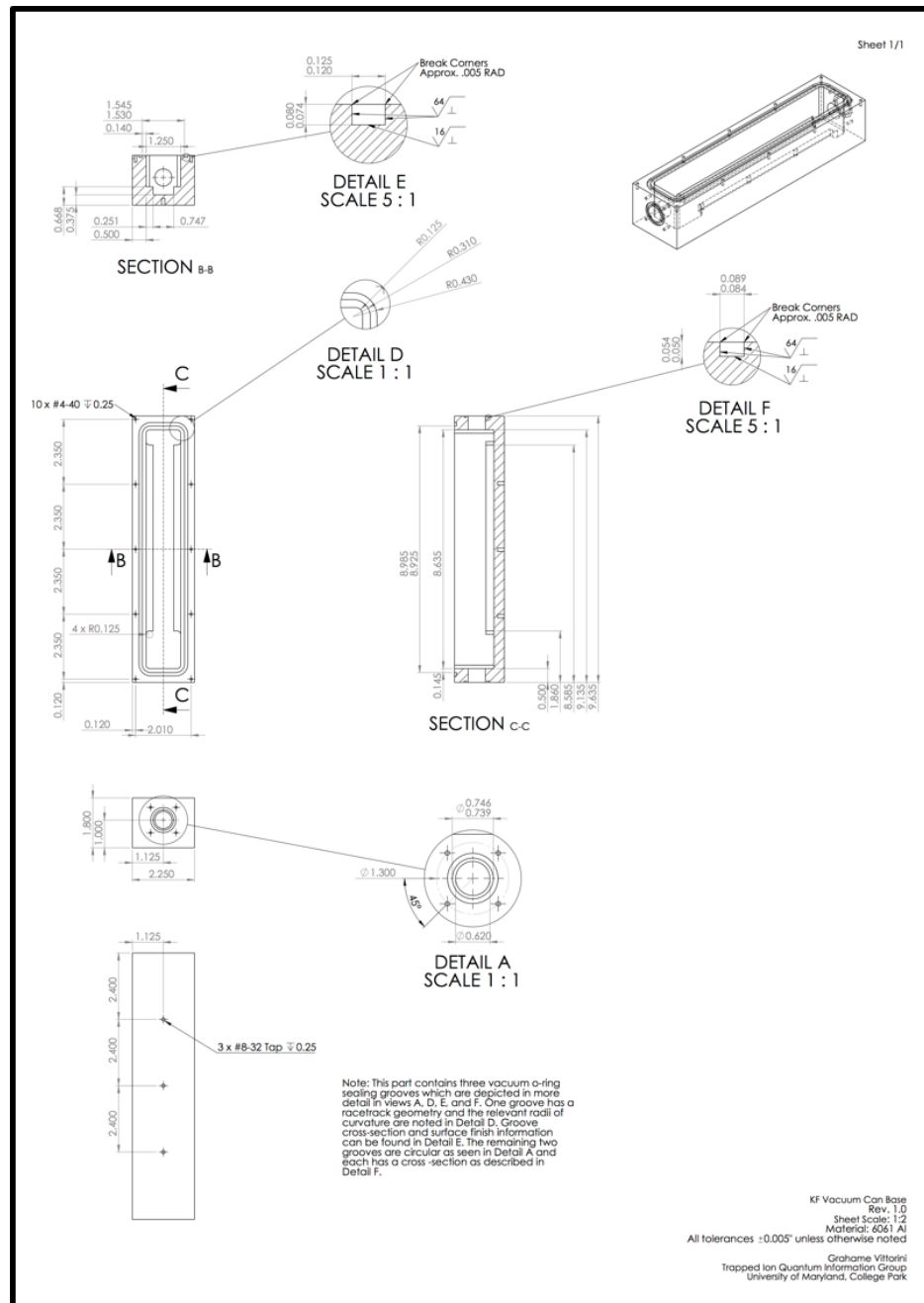


Figure B.5. KF Vacuum Chamber Base

B.6 KF Vacuum Chamber Lid

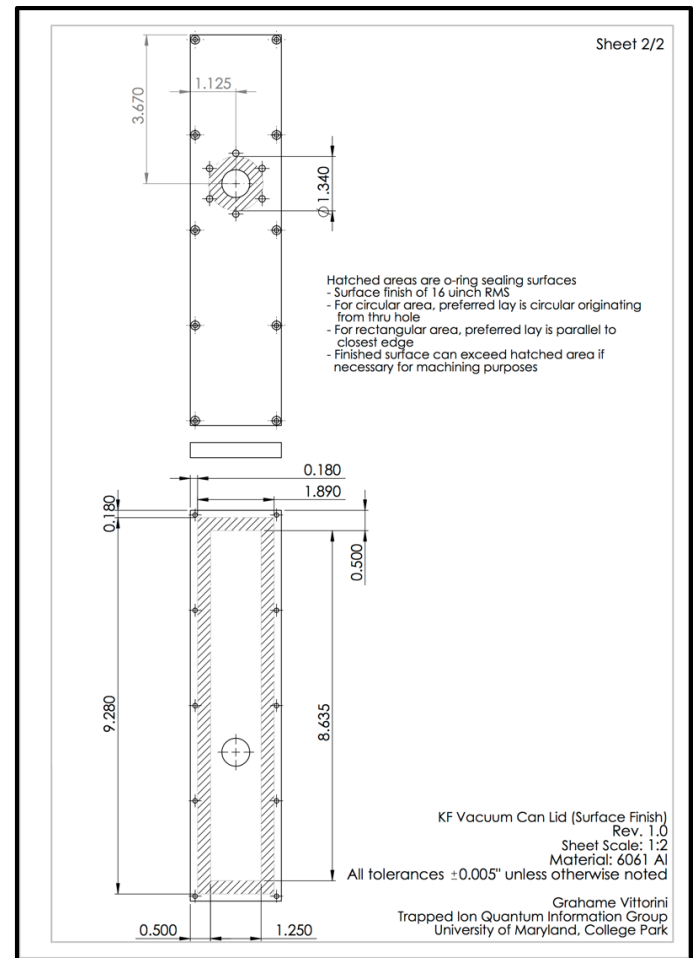
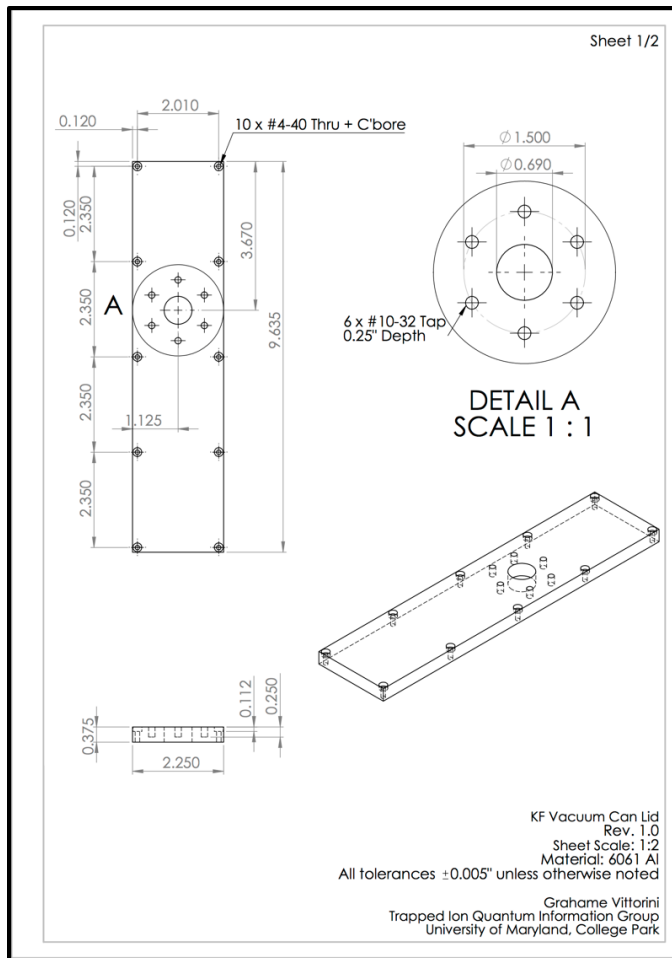


Figure B.6. KF Vacuum Chamber Lid

Appendix C Component Specifications & Manuals

C.1 Vacuum Components

- Mini-Ion Pump Manual:
http://www.agilent.com/cs/library/usermanuals/public/Miniature_2_ls_VacIon%20Pumps_Manual.pdf
- MiniVac Controller Manual:
<https://www.agilent.com/cs/library/usermanuals/Public/MiniVac%20Controller%2024%20Vdc.pdf>
- 26424-KE01 VAT KF-16 Vacuum Angle Valve:
<http://www.vatvalve.com/en/business/valves/product?id=26424-KE01>

C.2 Accu-Glass Products, Inc.

- UHV-compatible Butane Soldering Iron:
<https://accuglassproducts.com/product.php?productid=16164&cat=400&page=1>
- UHV In-Vacuum Solder:
<https://accuglassproducts.com/product.php?productid=16826&cat=400&page=1>

C.3 American Piezo Ceramics, Ltd.

- 42-1021 Piezoelectric Cylindrical Tube:
<https://www.americanpiezo.com/standard-products/piezo-tubes.html>

C.4 Lambda Research Optics Transfer Cavity Mirrors

- Both Transfer Cavity Mirrors Certificate of Conformance (Specifications):
<https://drive.google.com/open?id=0Bw9TeGv9XS9fOVFOX0N5bmVWbjg>

- Spherical Concave Mirror AR-Coating:
<https://drive.google.com/open?id=0Bw9TeV9XS9fZWJaZlBsaU1jTUE>
- Spherical Concave Mirror HR-Coating:
<https://drive.google.com/open?id=0Bw9TeV9XS9fXBhTHdfdUFzaE0>
- Plane Mirror AR-Coating:
<https://drive.google.com/open?id=0Bw9TeV9XS9fUkJmbUlmblkyYTg>
- Plane Mirror HR-Coating:
<https://drive.google.com/open?id=0Bw9TeV9XS9fOUR2aINST0tHRIE>

C.5 Semrock

- FF376-Di01-25x36 Long-pass Dichroic Filter:
<https://www.semrock.com/FilterDetails.aspx?id=FF376-Di01-25x36>
- FF510-Di02-25x36 Long-pass Dichroic Filter:
<https://www.semrock.com/FilterDetails.aspx?id=FF510-Di02-25x36>
- FF801-Di02-25x36 Long-pass Dichroic Filter:
<https://www.semrock.com/FilterDetails.aspx?id=FF801-Di02-25x36>
- MM3-311S-t6-25 MaxMirrors:
<https://www.semrock.com/FilterDetails.aspx?id=MM3-311S-t6-25>

C.6 Thorlabs

- PDA36A Si Amplified Photodetector with Adjustable Gain Manual:
<https://www.thorlabs.com/drawings/18266e5f0eae091f-380B7CD2-5056-0103-79C1374FEAC9094D/PDA36A-Manual.pdf>
- FB370-10 & FB400-10 Bandpass Filters:
https://www.thorlabs.com/newgrouppage9.cfm?objectgroup_id=1001
- BSW126 Broadband Non-Polarizing 50/50 Beamsplitter:
https://www.thorlabs.com/newgrouppage9.cfm?objectgroup_id=5111

- Fixed Focus APC Collimators:
https://www.thorlabs.com/newgrouppage9.cfm?objectgroup_id=1696
- Custom-Patch Single-Mode Fibers:
https://www.thorlabs.com/newgrouppage9.cfm?objectgroup_id=1634
- Glass Materials:
https://www.thorlabs.com/newgrouppage9.cfm?objectgroup_id=6973
- Anti-Reflectance Coatings:
https://www.thorlabs.com/NewGroupPage9.cfm?ObjectGroup_ID=5840

C.7 Allied Vision Technologies

- Guppy Camera Manual:
https://cdn.alliedvision.com/fileadmin/content/documents/products/cameras/Guppy/techman/Guppy_TechMan_en.pdf

References

- [1] H. J. Metcalf and P. van der Straten. *Laser Cooling and Trapping, Appendix C. Table C.1 Spectroscopic data for optical transitions used for laser cooling.* (Springer, 1999).
- [2] R. W. P. Drever, J. L. Hall, F. V. Kowalski, J. Hough, G. M. Ford, A. J. Munley, and H. Ward. “Laser Phase and Frequency Stabilization Using an Optical Resonator.” *Applied Physics B Photophysics and Laser Chemistry*, **31**(2):97-105. (1983). doi:10.1007/BF00702605
- [3] S. Kraft, A. Deninger, C. Trck, J. Fortgh, F. Lison, and C. Zimmermann. “Rubidium spectroscopy at 778-780 nm with a distributed feedback laser diode.” *Laser Physics Letters*, 2(2):71-76. (2005). doi:10.1002/lapl.200410155
- [4] K. B. MacAdam, A. Steinbach, and C. Wieman. “A narrow-band tunable diode laser system with grating feedback, and a saturated absorption spectrometer for Cs and Rb.” *American Journal of Physics*, **60**(12):1098-1111. (1992). doi:10.1119/1.16955
- [5] J. I. Kim, C. Y. Park, J. Y. Yeom, E. B. Kim, and T. H. Yoon. “Frequency-stabilized high-power violet laser diode with an ytterbium hollow-cathode lamp.” *Optics Letters*, **28**(4):245-247. (2003). doi:10.1007/s00340-009-3619-4
- [6] M. W. Lee, M. C. Jarratt, C. Marciniak, and M. J. Biercuk. “Frequency stabilization of a 369 nm diode laser by nonlinear spectroscopy of ytterbium ions in a discharge.” *Optics Express*, **22**(6):7210-7221. (2014). doi:10.1364/OE.22.007210
- [7] P. Bohlouli-Zanjani, K. Afrousheh, and J. D. D. Martin. “Optical transfer cavity stabilization using current-modulated injection-locked diode lasers.” *Review of Scientific Instruments*, **77**(9):093105. (2006). doi:10.1063/1.1144744

- [8] N. Seymour-Smith, P. Blythe, M. Keller, and W. Lange. “Fast scanning cavity offset lock for laser frequency drift stabilization.” *Review of Scientific Instruments*, **81**(7):075109. (2010). doi:10.1063/1.3455830
- [9] E. Riedle, S. H. Ashworth, J. T. Farrell Jr., and D. J. Nesbitt. “Stabilization and precise calibration of a continuous-wave difference frequency spectrometer by use of a simple transfer cavity.” *Review of Scientific Instruments*, **65**(1):42. (1994). doi:10.1063/1.1144744
- [10] S. Uetake, K. Matasubara, H. Ito, K. Hayasaka, and M. Hosokawa. “Frequency stability measurement of a transfer-cavity-stabilized diode laser by using an optical frequency comb.” *Applied Physics B*, **97**(2):413-419. (2009). doi:10.1007/s00340-009-3619-4
- [11] W. Z. Zhao, J. E. Simsarian, L. A. Orozco, and G. D. Sprouse. “A computer-based digital feedback control of frequency drift of multiple lasers.” *Review of Scientific Instruments*, **69**(11):3737. (1998). doi:10.1063/1.1149171
- [12] S. Olmschenk, K. C. Younge, D. L. Moehring, D. N. Matsukevich, P. Maunz, and C. Monroe. “Manipulation and detection of a trapped Yb^+ hyperfine qubit.” *Physical Review A*, **76**(5):052314. (2007). doi:10.1103/PhysRevA.76.052314
- [13] R. Islam, W. C. Campbell, T. Choi, S. M. Clark, S. Debnath, E. E. Edwards, B. Fields, D. Hayes, D. Hucul, I. V. Inlek, K. G. Johnson, S. Korenblit, A. Lee, K. W. Lee, T. A. Manning, D. N. Matsukevich, J. Mizrahi, Q. Quraishi, C. Senko, J. Smith, and C. Monroe. “Beat note stabilization of mode-locked lasers for quantum information processing.” *Optics Letters*, **39**(11):3238-3241. (2014). doi:10.1364/OL.39.003238
- [14] HighFinesse WSU-10 Wavemeter Manual. *HighFinesse*. <https://drive.google.com/file/d/0Bw9TeGv9XS9fckZZYnVLVjRGeVE/view?usp=sharing>

- [15] Vescent Photonics D2-Series Rb Quick Start Manual. *Vescent Photonics*.
http://www.vescent.com/manuals/doku.php?id=d2:quick_start
- [16] B. Edlén. “The refractive index of air.” *Metrologia*, **2**(2):71-80. (1966).
doi:10.1088/0026-1394/2/2/002
- [17] F. E. Jones. Journal of Research of the National Bureau of Standards 86:1, 27-32 (1980).
- [18] Cryogenic Division. *LNG Materials and Fluids*, National Bureau of Standards: Boulder, CO. (1977). [http://cryogenics.boulder.nist.gov/MPropsMAY/Invar\(Fe-36Ni\)/Invar_rev.htm](http://cryogenics.boulder.nist.gov/MPropsMAY/Invar(Fe-36Ni)/Invar_rev.htm)
- [19] “Optical Resonator Stability Diagram.” https://upload.wikimedia.org/wikipedia/commons/thumb/6/67/Laser_resonator_stability.svg/2000px-Laser_resonator_stability.svg.png
- [20] Fluke 179 True RMS Digital Multimeter Specifications. *Fluke*.
<http://en-us.fluke.com/products/digital-multimeters/fluke-179-digital-multimeter.html#techspecs>
- [21] Adjustable Gain Si Amplified Photodetector Manual. *Thorlabs*.
<https://www.thorlabs.com/drawings/c35a91f7ec65d47f-AFDCAA00-5056-0103-7947357E850E11C0/PDA36A-Manual.pdf>
- [22] O. Svelto. *Principles of Lasers*. (Springer, 2009), 5th ed.
- [23] D. A. Steck. *Classical and Modern Optics*. (revision 1.7.3, Feb. 2017).
Available at: <http://steck.us/teaching>
- [24] H. Kogelnik and T. Li. “Laser Beams and Resonators.” *Applied Optics*, **5**(10):1550-1567. (1966). doi:10.1364/AO.5.001550

- [25] J. R. Taylor. Chapter 8: Least-Squares Fitting, *An Introduction to Error Analysis: The Study of Uncertainties in Physical Measurements*. (University Science Books, 1982), 2nd ed.
- [26] D. W. Allan. “Statistics of Atomic Frequency Standards.” *Proceedings of the IEEE*, **54**(2):221-230. (1966). doi:10.1109/PROC.1966.4634
- [27] W. J. Riley and NIST Time and Frequency Division. “Handbook of Frequency Stability Analysis.” *National Institute of Standards and Technology Special Publication*, **1065**:136 pgs. (2008). <http://purl.access.gpo.gov/GPO/LPS119767>